Ocean Engineering 328 (2025) 120967

Contents lists available at ScienceDirect

Ocean Engineering

journal homepage: www.elsevier.com/locate/oceaneng

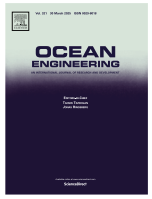

Research paper

Comparison of vector wave displacements from a moored and a drifting Spotter buoy—from an accidental Indian Ocean voyage

Thobani Hlophe [a,b,c,*], Paul H. Taylor [a,b], Jeff E. Hansen [a,b], Hugh Wolgamot [a,b], Michael V.W. Cuttler [a,b]

[a] School of Earth and Oceans, University of Western Australia, Perth, Western Australia, 6009, Australia
[b] Marine Energy Research Australia, Great Southern Marine Research Facility, Albany, Western Australia, 6330, Australia
[c] Department of Engineering Science, University of Oxford, Parks Road, Oxford, OX1 3PJ, UK

ARTICLE INFO

Keywords:
Mooring
Drifting
De-spiking
NewWave analysis
Nonlinear harmonics

ABSTRACT

Accurate measurement of ocean wave parameters is essential for marine engineering and environmental monitoring. This study analyses a unique dataset from a Sofar Spotter buoy that detached from its mooring in the Southern Indian Ocean. Originally deployed in 330 m deep water offshore of Perth, Western Australia, the buoy drifted southwest towards the Southern Ocean during the austral winter before returning to the coast, where it was eventually recovered. The complete deep-water displacement record, covering both moored and drifting modes, provides a rare opportunity to evaluate the Spotter buoy's performance across different configurations. Analysing ten months of data, we developed methods to detect and correct signal spikes, assessed how buoy motion affects measurement fidelity, and compared these findings to theoretical expectations. Additionally, we examined variations in buoy performance between moored and drifting modes, providing insights into buoy trajectories and movement patterns. This research advances the understanding of buoy-based wave measurement systems and lays a foundation for improving data accuracy in various oceanographic applications.

1. Introduction

The development of accurate and reliable wave forecast models relies heavily on the quality of measured data which can be used for forecast validation, model calibration or data assimilation. Accurate wave forecasts are essential for various offshore applications, including resource assessment and site selection for long-term (seasons to years) projects, system maintenance and optimisation over the medium term (weeks to months), and real-time decision-making for day-to-day operations. In recent years, the Sofar Spotter buoy (Sofar Ocean, 2024) has gained popularity due to its low cost and ease of deployment and recovery. However, as demonstrated in this study, recorded displacements can exhibit unrealistic spikes that distort the calculations of significant wave height H_s, spectral peak wave period T_p, and mean wave period T_z, among other important statistics, by the buoy's internal algorithms. Such inaccuracies could adversely affect decision-making based on short-term extrapolations of bulk wave statistics and hinder the validation of ocean wave models (see e.g., Hemer et al., 2017; Cuttler et al., 2020). While T_p is a naturally less stable parameter than T_z, it remains crucial for capturing the dominant energy-carrying waves in a wave spectrum, particularly in mixed sea states where multiple wave systems coexist. T_p is highly preferred for ship routing, offshore structure design, and forecasting long-period swells over T_z. Therefore, addressing and improving its accuracy alongside other parameters is important.

The Sofar Spotter buoy is a GNSS-based (Global Navigation Satellite System) wave buoy initially designed as a drifter, operating as a compact, solar-powered device that measures wave and weather data in real time. It can also be moored to hold station and report measurements from one location. Comparing its performance in moored and drifting modes provides valuable insights into how its wave measurements and motion dynamics vary under different conditions. Drifting buoys are particularly useful in the open ocean where mooring is challenging and costly (Veras Guimarães et al., 2018), effectively acting as Lagrangian sensors. In contrast, moored buoys are constrained by their mooring lines, which can introduce data artefacts related to the tension on the mooring line. Comparisons between moored Spotter buoys and a Datawell Directional Waverider-4 off Albany, Western Australia, have shown excellent agreement in measuring vertical ocean displacement, a key factor in bulk parameter calculations (Ding et al., 2024, 2025).

Few studies compare moored and drifting buoy performance, especially using large datasets that focus on individual wave motion

* Corresponding author.
E-mail address: thobani.hlophe@uwa.edu.au (T. Hlophe).

https://doi.org/10.1016/j.oceaneng.2025.120967
Received 20 November 2024; Received in revised form 1 March 2025; Accepted 11 March 2025
Available online 24 March 2025

rather than bulk statistics. This difficulty arises because of the way modern buoys work. Although the full motion in time is recorded and stored internally, this is typically not transmitted. Instead, the displacement record, often over 20–30 min, is analysed onboard the buoy with the resultant spectrum and bulk statistics transmitted onshore. Depending on the manufacturer, the onboard processing may or may not include quality control on the displacements. Obtaining the full displacement dataset requires recovering the buoy and downloading the data from the internal storage. For open ocean drifting studies, buoys are often not deployed for long durations due to the risk of loss, which limits the ability to analyse the full displacement record, as done in this study. From a bulk statistics viewpoint, Hisaki (2021) found good agreement between H_s and T_z observations from a moored GNSS buoy and a drifting accelerometer-based buoy, despite differences in sensing technologies, attributing the discrepancies to spatial variability.

This paper uses a unique dataset to explore the similarities and differences between a moored and drifting Spotter buoy. The 10-month dataset we analysed was obtained from a buoy initially moored in deep water (330 m) off the coast of Perth, Western Australia. After four months, the buoy broke free from its mooring and then drifted ~ 800 km SW towards the Southern Ocean before drifting back towards Perth where it was recovered. Since the buoy was recovered, we can analyse the complete displacement record and compare the buoy's behaviour in both moored and drifting modes. Notably, the full dataset except for the period immediately before it was recovered near the coast (which is excluded from our analysis) was in deep water for the prevailing swell conditions such that finite depth effects on the waves are absent.

We address the comparison with two main objectives. First, we assess data quality by quantifying the occurrence of erroneous measurements, specifically spikes in the displacement record. These spikes are believed to result from the buoy temporarily losing GNSS satellite lock, possibly when overtopped by waves. Such errors can lead to substantial overestimations of H_s, sometimes doubling the corrected value obtained after spike removal, thereby misrepresenting sea states. Similarly, the erroneous buoy-calculated T_p can exceed the expected value by a factor of four. By comparing the prevalence of spikes when the buoy was moored versus drifting, we evaluate the potential impact of mooring on data quality.

Signal spikes exhibiting a 'saw-tooth' pattern have been reported by Björkqvist et al. (2016) in Datawell G4 buoy data. In the frequency domain, they observed a f^{-2} trend for $f \leq 0.07$ Hz and scaled the spectrum by f^2, yielding a constant value in that range, which was then subtracted from the entire spectrum. However, they recommended this approach for simple analysis. More recently, Dhoop et al. (2024) demonstrated that ignoring the corrupted portion of the heave record is effective, even for records as short as six minutes. Furthermore, statistics derived from such short records have been used reliably in forward wave-by-wave propagation models (see e.g., Hlophe et al., 2023; Chen et al., 2024).

This study introduces a robust method to detect and remove spikes from the buoys 3D displacement signals. Our approach employs predefined thresholds based on displacement from the mean-free surface, time-series curvature, and expected maximum periods. This method effectively restores the accuracy of wave measurements, ensuring that the derived bulk parameters more reliably represent actual sea conditions.

The second objective is to compare the motions of a moored versus drifting buoy and evaluate them against theoretical expectations. First, we examine buoy behaviour using linear wave theory, noting that a drifting buoy typically follows fluid particle motion more closely than a moored buoy. We then apply NewWave-type analysis (see e.g., Lindgren, 1970; Tromans et al., 1991; Jonathan and Taylor, 1997; Zhao et al., 2018; Ding et al., 2023) to investigate the average properties of the highest 10 % of waves in 10-h continuous records with stable wave conditions. This comparison, conducted for both moored and drifting cases, provides insight into the buoy's response under different operational conditions and highlights the influence of its motion on recorded wave data from both linear and nonlinear perspectives.

The paper is organised as follows: Section 2 describes the buoy deployment and presents bulk parameters derived from displacement time histories. Additionally, an algorithm for detecting and removing erroneous spikes is presented. Section 3 explores the linear behaviour based on theoretical relationships described using the auto-spectrum and cross-spectrum. Section 4 discusses the NewWave-type analysis and compares buoy performance in moored and drifting configurations. Finally, Section 5 summarises the findings.

2. Buoy deployment, voyage, and measured parameters

Observations from a single Sofar Spotter buoy from 16 October 2019 to 1 September 2020 are analysed in this paper based on the recorded buoy displacements (at 2.5 Hz). The wave buoy was initially deployed in 330 m of water in the Indian Ocean at Perth Canyon, approximately −31.954° latitude and 115.015° longitude—roughly 80 km west of Perth, Western Australia (see Fig. 2a).

The buoy was moored using the mooring line system sketched in Fig. 1. This system comprised a 1000 m polypropylene rope extending from an anchor (60 kg) up through a series of bullet-shaped floats on the ocean surface. These floats provided sufficient buoyancy to keep the top of the mooring at the surface, even in the presence of the strong Leeuwin Current, while minimising drag by reducing the surface area normal to the current. The in-line bullet floats were then connected to the buoy by a 30 m polypropylene rope that included small lead beads to make it negatively buoyant (to act as a catenary in the last portion of the mooring).

Fig. 2 shows a map of Western Australia and the buoy's deployment location, plotted from the onboard GNSS coordinates saved by the buoy at 10-min intervals. As seen in Fig. 2b, while moored, the buoy spent

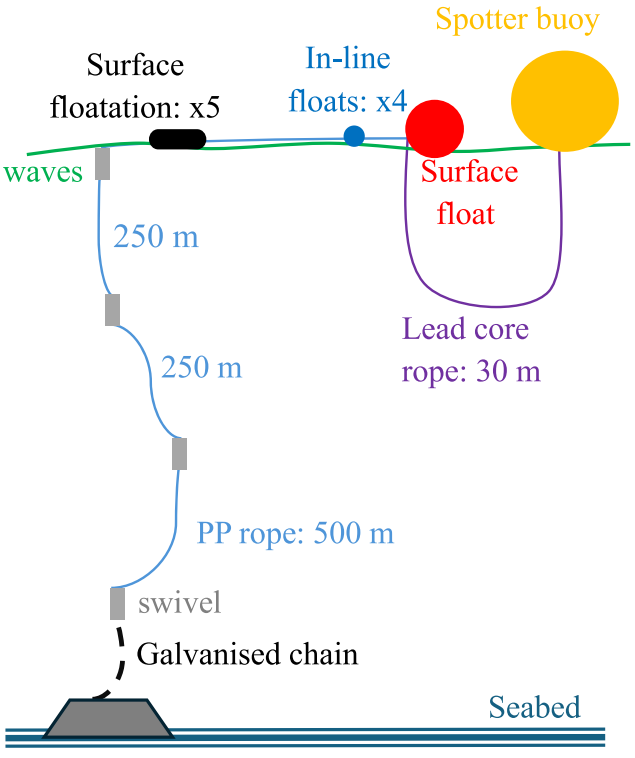

Fig. 1. Illustration of the mooring system used to anchor the Spotter buoy to the seabed at a depth of 330 m in Perth Canyon, Western Australia. The system includes 500 m of 7 mm thick polypropylene (PP) rope, with the remaining sections using 6 mm thick rope. Each of the bullet-shaped surface floats provided 20 kg of buoyancy.

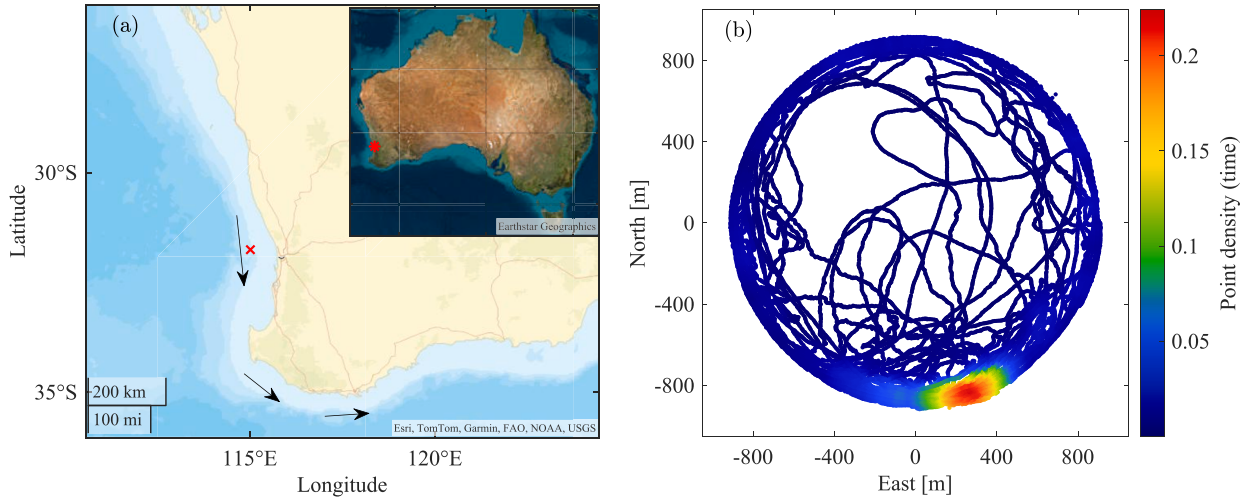

Fig. 2. (a) Map showing southwest Western Australia, with an inset of Australia highlighting the location of Perth, marked by a red asterisk (∗). Perth Canyon, located approximately 80 km west of Perth and marked by a red cross (×), is the deployment site of the Spotter buoy. The arrows (→) represent the position and direction of flow of the Leeuwin Current. (b) Heat map illustrating the positions of the Spotter buoy during the moored period, with (0,0) corresponding to (×).

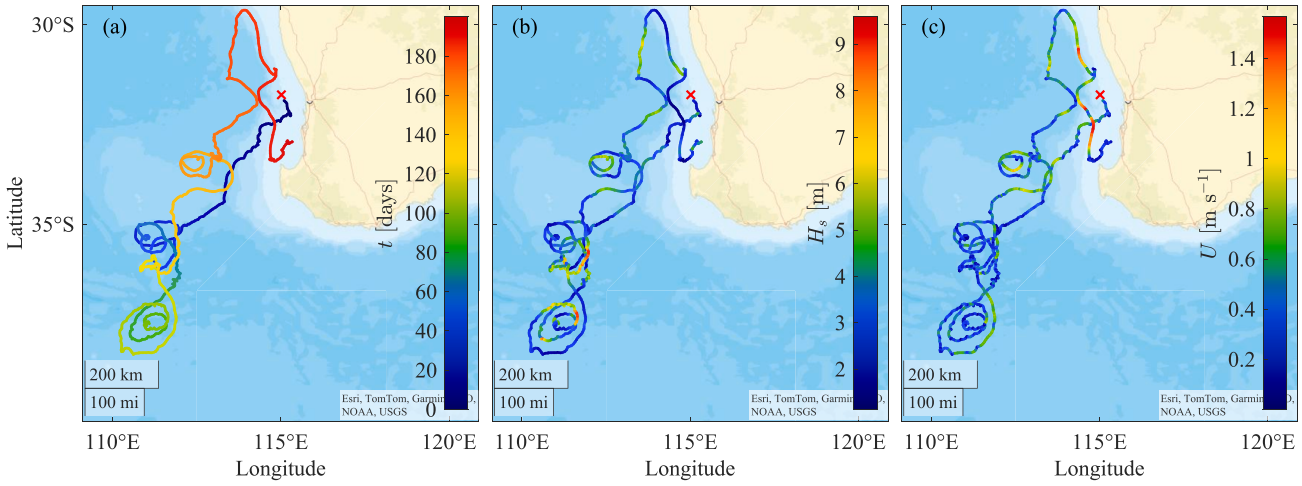

Fig. 3. Trajectory of the buoy during its voyage, plotted as functions of (a) time t, (b) significant wave height H_s, and (c) drift speed U. The cross (×) marks the origin of the buoy at Perth Canyon.

a significant amount of time south-southeast of the centre of the watch circle. This is consistent with the direction of the Leeuwin Current, a warm ocean current that flows southward along the western coast of Australia (see e.g., Cresswell and Golding, 1980). The current curves around Cape Leeuwin and continues into the southern waters of Australia, with its influence extending as far as Tasmania.

Just over 120 days after the deployment, on 13 February 2020, the mooring line broke ∼ 0.5 m below the buoy due to chafing in the lead core catenary, as observed upon recovery. The buoy then drifted for over 200 days, to a maximum straight-line distance from the mooring location of ∼ 815 km (southwest) before returning and being retrieved from Preston Beach, approximately 120 km south of Perth, on 3 September 2020. Fig. 3 shows the convoluted trajectory of the buoy during its 5540 km voyage. The panels of Fig. 3 illustrate the time from the beginning of drift in (a), significant wave height (H_s, traditionally the average of the highest one-third of the zero-crossing wave heights, but in modern analysis, as well as in this work, taken as 4× the standard deviation of the surface elevation away from the mean) in (b), and the buoy's drift speed in (c), calculated from finite differencing of the GNSS-based positions. The buoy occasionally encountered extreme sea states with $H_s \sim 10$ m. The path also reveals three large loops in the ocean, indicating that the buoy was carried by currents around oceanic eddies. The first loop, occurring as the buoy moved away from the mooring location, was clockwise, while the other two loops on its return were counterclockwise. It is important to note that during drifting, the buoy was assumed to behave as a true Lagrangian sensor, moving as a water particle on the free surface would.

In addition to saving its geographic position at 10-min intervals, the Spotter buoy records its 3D displacement: easting, northing, and heave (vertical) at 2.5 Hz, which are treated as the ocean surface displacement. GNSS data are used to determine the buoy's horizontal displacement (easting and northing) by calculating changes in geographic coordinates over time. The vertical displacement is derived by time integrating the buoy's vertical velocity as determined by the Doppler shift of the satellite signals. From 30-min records of the ocean surface, referred to herein as sea states, based on the expected stationarity in wave conditions, the buoy processes the measured displacements to provide spectral information and bulk statistics onboard, applying a bandpass filter with cut-off periods of 1 and 30 s, but the buoy itself is designed to sense waves up to 33 s long. In 'standard' mode, the buoy transmits half-hourly estimates of bulk statistics and its geographical location at hourly intervals, i.e., the buoy transmits statistical data for a pair of sea states hourly

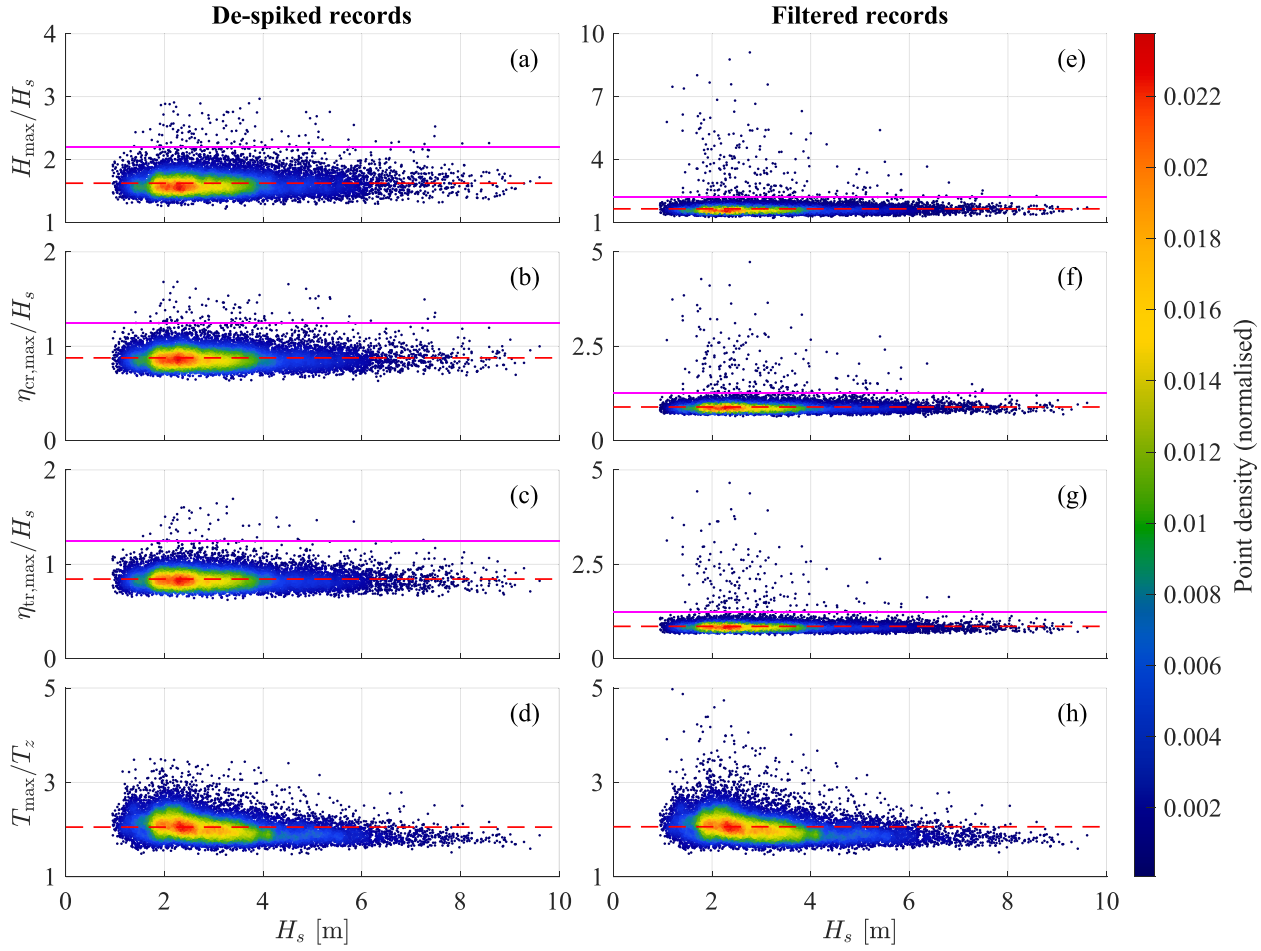

Fig. 4. Ratios of extreme (a,e) wave height H_{max}/H_s, (b,f) crest elevation $\eta_{cr,max}/H_s$, (c,g) trough depression $\eta_{tr,max}/H_s$, and (d,h) period T_{max}/T_z observed in 30-min sea states over the entire 321-day record (i.e., both moored and drifting data). The dashed lines represent mean values for all sea states, while the solid lines indicate the thresholds of extreme events: (a,e) $H_{max} = 2.2H_s$ and (b,c,f,g) $|\eta|_{max} = 1.25H_s$. The left panels show bulk parameters from de-spiked time histories, while the right panels use filtered-only records.

(Sofar Ocean, 2024). The actual time series of ocean displacements is saved onto an SD card, which can be retrieved manually and analysed later. This work is thus based on the large dataset retrieved when the buoy was recovered.

2.1. Bulk wave statistics

The analysis in this section use the heave displacement time history, denoted η. Although processed data are used throughout this work, we have verified the consistency of our calculations by comparing them with the buoy's onboard processing. Specifically, we repeated the bulk wave parameter calculations using the raw time series data retrieved from the buoy's SD card, without pre-processing. The results showed excellent agreement, confirming that the buoy's onboard computations align closely with our independent analysis.

The raw data show a noticeable presence of high-frequency content. To mitigate this, all records are henceforth analysed within the effective wave frequency range $[f_{min}, f_{max}] = [1/30, 1/3]$ Hz to reduce noise contamination. To achieve this, a band-pass filter with sinusoidal ramping is applied to the Fourier components of time-series data, ensuring smooth attenuation of frequency components outside the target range while preserving the dominant wave signals. The filter is designed with a transition (ramp) region at both the lower and upper-frequency bounds, implemented using a sine window function. The ramp width is set to 5 % of the total frequency range, providing gradual transitions instead of abrupt cut-offs at f_{min} and f_{max}. The filter follows a 0–0.5–1–1–0.5–0 profile, where the amplitude begins at 0, rises to 0.5 at f_{min}, reaches 1 within the passband, then symmetrically decreases to 0.5 at f_{max} before tapering to 0 outside the range. Thus, it remains flat at 1 for 90 % of the passband. This ensures a smooth transition while preserving key wave components within the selected frequency range, minimising spectral leakage and ensuring a physically meaningful representation of the wave signals.

A zero-crossing analysis is performed for each sea state (30 min) to determine sets of individual wave heights and periods. Both up-crossings and down-crossings are used, and where necessary, the average of these two is employed. From this, the largest wave height H_{max}, period T_{max}, crest elevation $\eta_{cr,max}$, and trough depression $\eta_{tr,max}$ are identified for each sea state. The significant wave height $H_s = 4\sigma_\eta$ is defined through the time-domain RMS standard deviation σ_η of the η record. The mean period T_z is calculated from zero-crossings.

Fig. 4 displays scatter plots of dimensionless bulk parameters, comparing de-spiked records with 'filtered' records. The left-hand panels use de-spiked records, while the right-hand panels use the raw records filtered over the new f band. All records are filtered over the same frequency range and are normalised using the same H_s or T_z from the de-spiked records. The dashed horizontal lines in the panels indicate averages, with the average for $H_{max}/H_s = 1.62$, close to the expected value of 1.6 in Rayleigh-distributed waves. The solid horizontal lines indicate thresholds for rogue wave events. A rogue or freak wave is generally defined as a wave exceeding twice the significant wave height (Holthuijsen, 2010, §4). Consistent with previous authors, these thresholds are

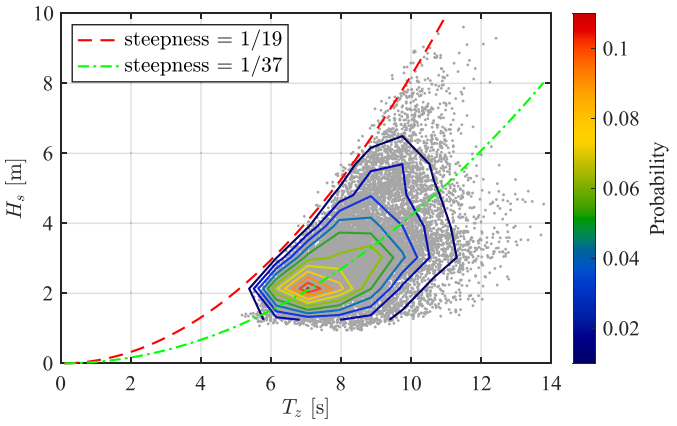

Fig. 5. Scatter plot of significant wave height H_s versus mean period T_z for all 30-min sea states over 321 days. Contour lines indicate the probability of occurrence. The red, dashed line represents the limiting steepness, and the green, dash-dotted line corresponds to the most probable sea-state steepness.

wave heights $H/H_s \geq 2.2$ (e.g., Heller, 2006; Kurniawan et al., 2022) and wave displacements $\eta/H_s \geq 1.25$ (e.g., Dysthe et al., 2008; Baschek and Imai, 2011; Kurniawan et al., 2022). Note, however, that there is no unique definition for rogue waves; for instance, Dysthe et al. (2008); Baschek and Imai (2011) use a threshold of $H/H_s \geq 2$.

The $H/H_s \geq 2.2$ and $\eta/H_s \geq 1.25$ thresholds, along with extreme wave periods $T/T_z > 3.5$ used in Fig. 4, are later employed in Section 2.2 in an algorithm that systematically detects and removes spikes from a time-series wave record. The figure demonstrates that spikes can significantly skew bulk statistics, potentially affecting decision-making that relies on short-term forecasts (extrapolations) of wave conditions.

For the remainder of this section, de-spiked records will be used. Fig. 5 depicts a scatter plot of T_z versus H_s from a combination of moored and drifting records. Contour lines overlaid on the scatter plot indicate the probability of occurrence, providing insights into the most frequently observed sea states. The ranges of T_z and H_s are each divided into 10 bins. The most probable sea state has $T_z = 7.15$ s and $H_s = 2.16$ m. The dashed line in the figure represents the limiting wave steepness, obtained from fitting the data (see Tucker and Pitt, 2001, §6.3), corresponding to a steepness ratio $H_s/\lambda = 1/19$ and steepness $k_z H_s = 0.34$, where H_s is the wave height, λ is the wavelength and $k_z = 2\pi/\lambda$ is the wavenumber, based on T_z. This line delineates the boundary beyond which wave conditions are limited by breaking. The dash-dotted line corresponds to the mean wave steepness, with a steepness ratio of 1/37, representing the most probable or average wave steepness observed in the dataset. The limiting steepness is a theoretical bound set by wave breaking, while the most probable steepness provides a more realistic measure of typical wave conditions.

After carefully removing spikes (see Section 2.2), calculations of wave height become less contaminated. For instance, the time series of H_s in Fig. 6a is particularly free from rapid fluctuations, in line with the fact that waves are generated by distant storms that last for several hours. Consistent with the onset of the Austral winter, waves became significantly larger around June as the storm intensity and rate of occurrence in the Southern Ocean increased. (see e.g., Cuttler et al., 2020). Fig. 6b shows the number of waves flagged as spikes in each sea state based on height: $H > 2.2H_s$, with the wave steepness (calculated as $k_z H_s$) plotted on a separate right-hand y-axis. Although including spikes impacts bulk statistics, there is often only a single large wave in a 30-min record, and only occasionally more than three spikes. Thus, sufficient data should be left to calculate and report accurate sea-state bulk parameters after removing spikes. The figure also reveals some correlation between high wave steepness and large events, particularly during the moored period.

2.2. Detection and removal of erroneous spikes

Removing spikes before calculating bulk parameters is crucial as it significantly skews important bulk statistics, as illustrated in Fig. 7. For this paper, a 'spike' is the largest displacement (positive or negative) in a zero-crossing wave that meets at least one of the detection criteria described below. Importantly, a combination of up- and down-crossings is considered, allowing for the detection of up to three spikes in three successive zero-crossings.

The criteria used for spike detection are based on the wave displacement from the mean and the zero-crossing mean period T_z. Given that the buoy measures motion in three degrees of freedom (DoFs), an analogous parameter to H_s for heave is computed, denoted $\hat{H}_s$. Specifically, $\hat{H}_s = 4\sigma_\zeta$, where σ_ζ is the standard deviation of the

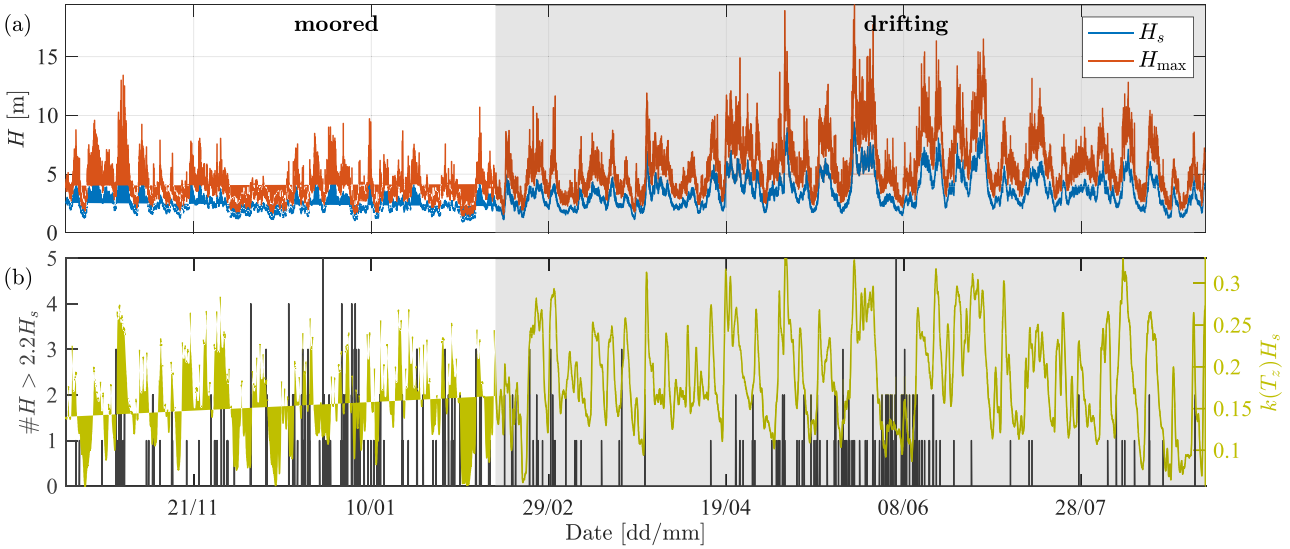

Fig. 6. (a) Time series of wave heights (H_s and H_{max}) for all 30-min (de-spiked) sea states observed by the buoy while moored and drifting. (b) Time series of zero-crossing wave heights exceeding $2.2H_s$ in each (filtered, i.e., non-de-spiked) sea state, plotted with the associated wave steepness ($k_z H_s$, on the right y-axis). The grey shading indicates the period when the buoy was drifting.

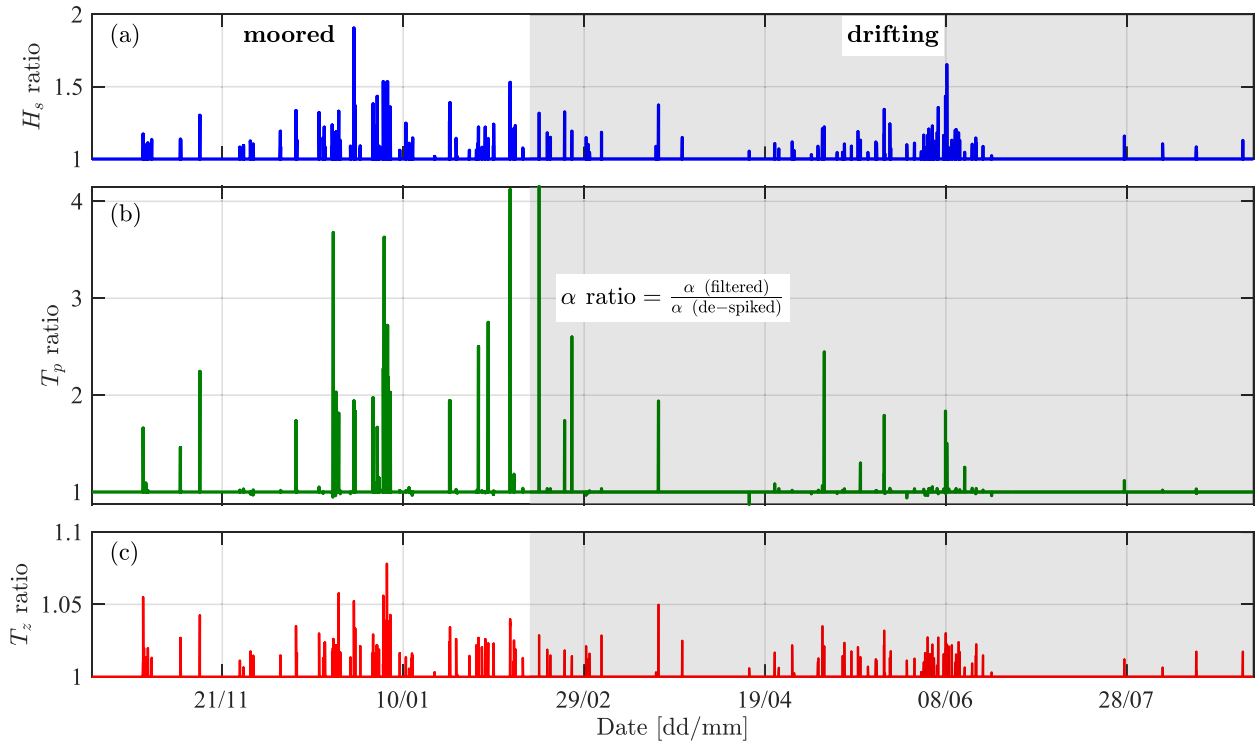

Fig. 7. Ratios of significant wave height significant wave height H_s, peak period T_p and mean wave period T_z between the filtered-only records and the corresponding de-spiked records (this paper). Shaded regions indicate the drifting period, with annotations marking the moored and drifting modes. The α in (b) is a dummy parameter for the expression used to evaluate the ratios in (a–c).

signal ζ, corresponding to easting (X), northing (Y) or heave (η). The mean period T_z is solely calculated from the heave signal because horizontal displacements can be smaller and noisier depending on the relative alignment with the mean wave direction. Recall that all signals are band-pass filtered over [1/30, 1/3] Hz to minimise noise effects. Spike detection and removal are based on iterative updates of T_z and $\hat{H}_s$. To ensure effective removal, 30 s' worth of data points on either side of each detected spike are discarded, a period chosen based on the lowest frequency of cut-off used in the buoy's onboard data analysis.

The first criterion identifies a spike based on crest-trough displacement or vice versa. A wave with a 'height' of $\hat{H} > 2.2\hat{H}_s$ is flagged for further analysis, consistent with previous studies (Heller, 2006; Baschek and Imai, 2011; Kurniawan et al., 2022). The accompanying test involves checking the time-series curvature $\mathcal{K}$, calculated using finite differencing, with a threshold of five standard deviations, $\sigma_{\mathcal{K}}$. The curvature is more sensitive than the slope and is hence preferred. The $5\sigma_{\mathcal{K}}$ for the curvature is chosen for its association with the large spikes of particular concern. Waves with $\hat{H} > 3\hat{H}_s$ are outright classified as spikes. Therefore, any 'rogue waves' remaining in the record are those with heights up to $3\hat{H}_s$. The second criterion also includes a scan of individual crests and troughs using thresholds of $1.25\hat{H}_s$ and $1.7\hat{H}_s$ for displacement, with the former accompanied by the same curvature test. The final criterion examines zero-crossing periods, identifying all waves longer than $3.5T_z$ or 30 s as spikes. Although Kurniawan et al. (2022) suggested a threshold of $3T_z$, it was found to detect too many subtle spikes in this study. As a result, the threshold was subsequently relaxed to $3.5T_z$. Eq. (2.1) summarises the detection criteria used:

$$\begin{cases} \text{Criterion 1} \equiv \left(\hat{H} > 2.20\hat{H}_s \wedge \mathcal{K} > 5\sigma_{\mathcal{K}}\right) \vee \left(\hat{H} > 3.0\hat{H}_s\right), \\ \text{Criterion 2} \equiv \left(|\hat{\eta}| > 1.25\hat{H}_s \wedge \mathcal{K} > 5\sigma_{\mathcal{K}}\right) \vee \left(|\hat{\eta}| > 1.7\hat{H}_s\right), \\ \text{Criterion 3} \equiv T > \min\left(3.5T_z, 30\right), \end{cases} \tag{2.1}$$

where $\wedge$ denotes logical *and* and $\vee$ denotes logical *or*. Waves that satisfy these criteria are removed from the record in an iterative process. The key steps of the de-spiking algorithm are outlined as follows:

1. Initialisation: Load the time-series signals $\zeta \in \{X, Y, \eta\}$ and η, and compute initial estimates for $\hat{H}_s = 4\sigma_\zeta$ and T_z (from η).
2. Zero-crossings identification: Detect all zero-crossings (both up and down) within the time series to define individual wave segments.
3. Spike detection: For each ζ wave segment, apply the criteria outlined in Eq. (2.1) to identify spikes based on displacement magnitude and curvature.
4. Data removal: Remove identified spikes along with a buffer of 30 s on either side to prevent contamination of surrounding data.
5. Parameter update: Recalculate wave parameters ($\hat{H}_s$ and T_z) using the cleaned data.
6. Iteration: Repeat steps 3–5 until convergence is achieved, typically within three iterations.

The full pseudocode implementation of the de-spiking procedure is provided in Appendix A.

Fig. 8 illustrates a heave record from the sea state with the largest number (10) of identified spikes, observed between 12:30 and 13:00 on 5 January 2020 when the buoy was still moored. Panel (a) shows the entire time history, with spikes marked by vertical red lines. The shaded region indicates where spikes occur, with a zoomed-in view provided in panel (b). The relative heights of the spikes, especially those occurring after 5 min, appear unrealistic. Panel (c) displays the wavelet transform of the signal, highlighting spikes with disproportionately high energy at low frequencies (long periods). Panel (d) presents the 1D power spectral density (PSD) before and after spike removal, showing errors of 143 % and 53 % in the spectral peak wave period T_p and H_s, respectively.

A quantitative comparison of spike occurrence is conducted using the first 120 days of buoy moored and drifting periods, equating to 5760 30-min sea states for each case. Note that the 120-day duration is based on the moored period, which is shorter than the available drifting period. Seasonal variation bias is not considered here. Spikes are detected in easting, northing, and heave signals based on each criterion in Eq. (2.1) and their combinations. The results are shown in Fig. 9, which

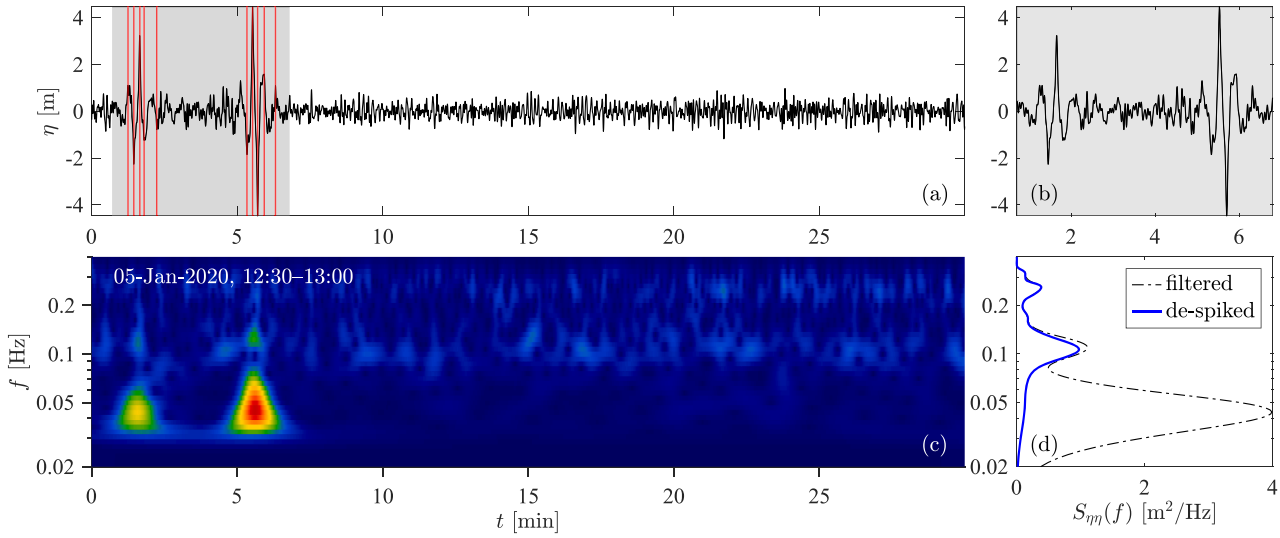

Fig. 8. (a) Heave, η, time history of the spikiest sea state on 5 January 2020, with red lines indicating crests and troughs identified as spikes. (b) Close-up view of the region with spikes. (c) Wavelet transform of the heave displacements; red denotes high energy. (d) PSDs, $S_{\eta\eta}(f)$, computed from the filtered heave record with spikes ($0 \le t < 30$ min) and de-spiked record ($t > 6.8$ min).

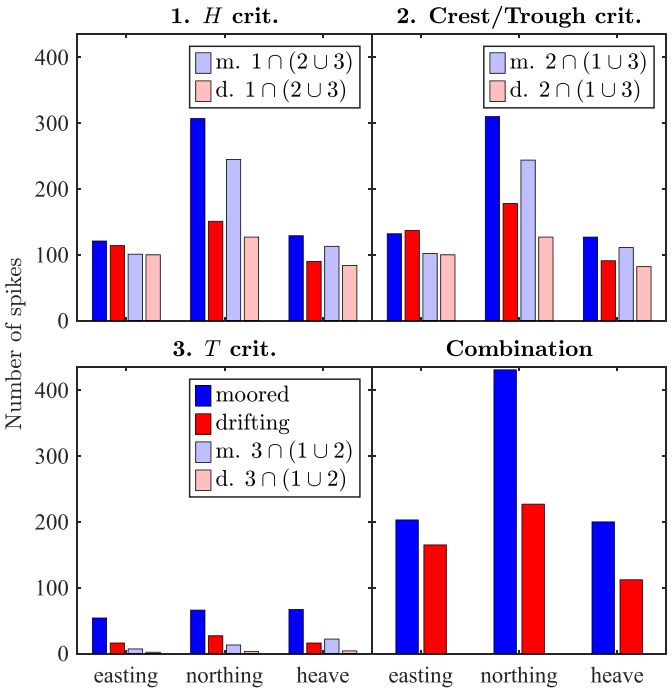

Fig. 9. Bar charts illustrating the number of detected spikes based on the criteria outlined in Eq. (2.1) for easting, northing, and heave displacement records during both moored and drifting modes. The pale-coloured bars represent the intersections of each criterion with the other two. The labels 'm.' and 'd.' denote moored and drifting conditions, respectively. The term 'Combination' refers to the union of all criteria. Here, ∩ indicates the intersection and ∪ represents the union of the criteria.

compares the number of detected spikes across different DoFs and criteria. Criteria 1 and 2 are the most significant, capturing largely the same spikes, while Criterion 3 identifies additional and mostly unique spikes. As anticipated, horizontal displacements, especially in northing during the moored period, exhibit significantly more spikes due to the buoy's restricted southward movement (due to the buoy being constrained by the mooring in the southerly directed Leeuwin Current).

As waves become steeper, the probability of wave breaking increases. This process may cause the breaker to either overtop the buoy or force it to move violently in the horizontal plane. Such movements can result in erroneous horizontal measurements, appearing as large events or discontinuities detectable by the curvature test.

Sea states with steepness values of $0.05 \le k_z H_s \le 0.35$ are grouped into bins with a width of 0.05. Fig. 10 illustrates the relationship between the number of spikes and sea-state steepness. The general pattern observed is consistent with that shown in Fig. 9. Notably, there is a rapid increase in the number of spikes with wave steepness, particularly for the moored mode in the northing direction and to a lesser extent in the easting direction. For heave measurements, no clear pattern emerges, either for moored and drifting modes. The easting and northing data from the drifting case show an increase in spikes up to 0.1 spikes per 30-min sea state for $k_z H_s \ge 0.25$, likely due to wave breaking over the buoy.

Overall, the occurrence of spikes is relatively low for both moored and drifting portions of the dataset. For a moored Spotter buoy, a single spike is typically expected within an hour in sea states with the highest steepness considered here, $k_z H_s \in [0.3, 0.35)$, while for a drifting buoy in sea states of similar steepness, a single spike is expected approximately every five hours. However, it remains crucial to examine individual sea states to identify records that may be excessively affected by spikes, rendering a portion of the data unusable. Fig. 11 displays the number of spikes per sea state for each of the three DoFs, overlaid with wave steepness. This figure reaffirms the dependence of spike occurrence on steepness in the horizontal displacements. Notably, a single spike is common, with records rarely containing more than three spikes. The highest number of spikes observed in a single 30-min record in this dataset is 10, as previously discussed and shown in Fig. 8a. The tendency for spikes to cluster in packets makes their removal and the recovery of usable segments of the records feasible.

It is important to note that while T_z and H_s are calculated in the time domain and remain unaffected by discontinuities after removing spike segments, directional bulk parameters calculated using the Fourier transform (see e.g., Mitsuyasu et al., 1980; Long, 1980) are sensitive to discontinuities. The use of the Fourier transform on discontinuous signals can cause spectral leakage, where energy from one frequency component contaminates others, leading to inaccuracies in the frequency spectrum. Consequently, for Fourier-based analysis, it is crucial to use long, continuous segments of the record that remain after spike removal.

Fig. 12 illustrates the percentage of usable data remaining from both heave and 3-DoF records after removing spikes and excluding a ±30 s window around each spike. Panel (a) displays the discontinuous records,

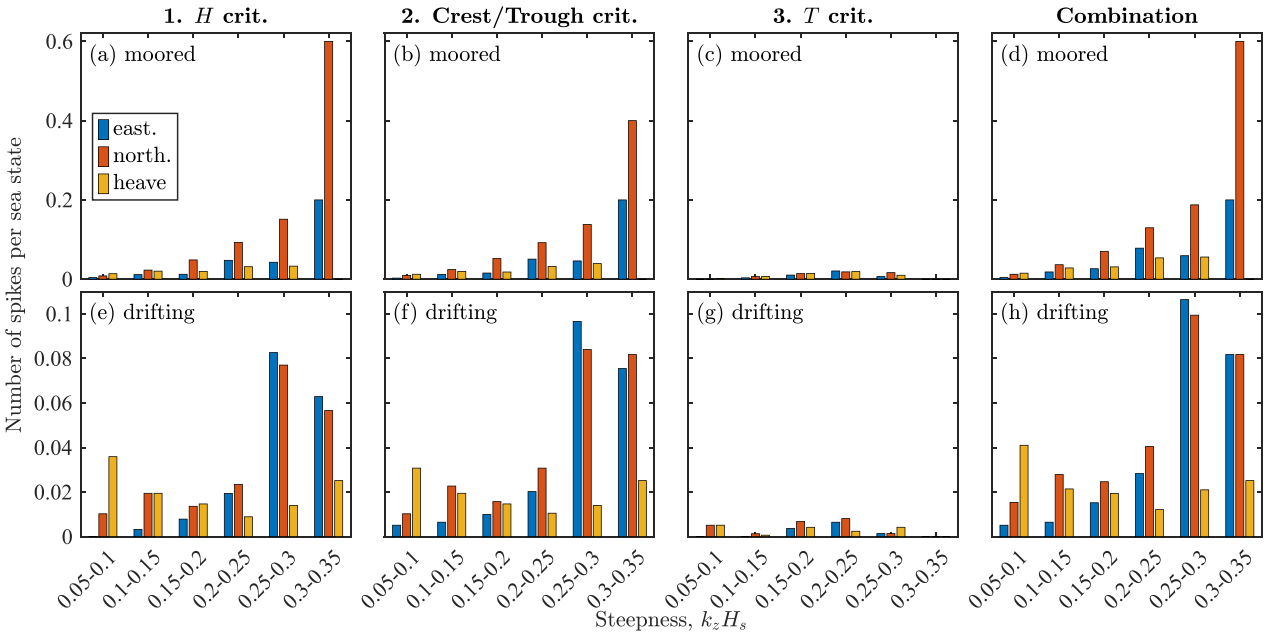

Fig. 10. Number of spikes per sea state (30 min) as a function of wave steepness k_zH_s for easting, northing, and heave records during (a–d) moored and (e–h) drifting. 'Combination' refers to the union of all the criteria. Note the different vertical scales for moored and drifting.

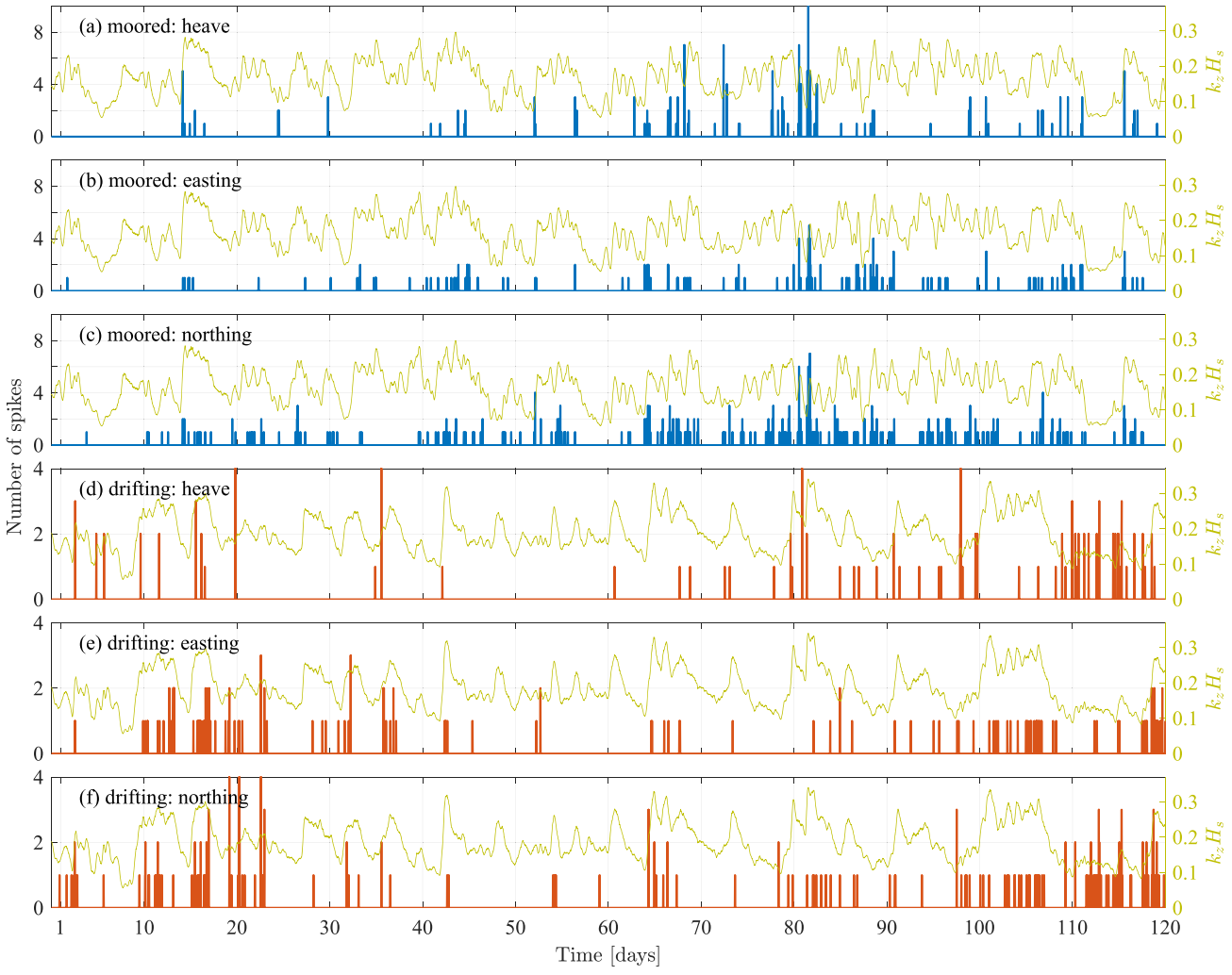

Fig. 11. Time series of the total number of spikes and associated steepness k_zH_s in each 30-min sea state, for each of the three translational degrees of freedom (heave, easting, northing), over the first 120 days when the buoy was (a–c) moored, and (d–f) drifting.

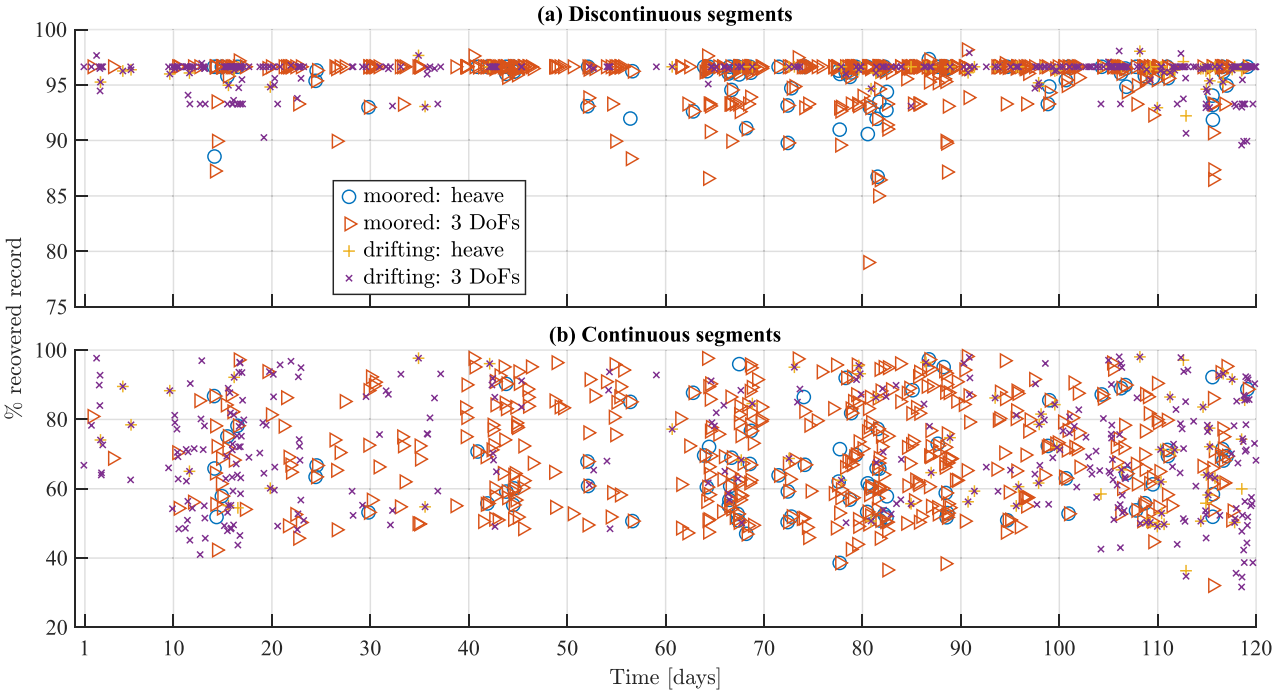

Fig. 12. Percentages (%) of recovered records after de-spiking each sea-state (30 min) record, in heave and a union of all three degrees of freedom (DoFs). (a) % of discontinuous segments and (b) % of the longest continuous segments, after discarding regions around spikes. Sea states without spikes are not shown.

which are suitable for time-domain analysis, while panel (b) shows continuous segments, which are ideal for frequency-domain calculations. Although the continuous segments are generally shorter than the discontinuous records, they still typically represent over 40 % of the original record—sufficient for PSD estimation (see e.g., Hlophe et al., 2023; Dhoop et al., 2024). It is worth noting that the 3-DoF records are shorter than the heave records because spikes do not always occur simultaneously across all 3 DoFs. Consequently, the discarded segments are combined across the 3-DoF records, leading to shorter usable segments compared to the heave-only case.

Table 1
Mean and standard deviation of time-series bulk wave parameters shown in Fig. 13a, for both moored and drifting buoy cases.

Parameter	Moored		Drifting	
	mean	std	mean	std
H_s [m]	4.83	0.233	4.89	0.305
T_z [s]	8.57	0.357	8.86	0.317
$\overline{\theta}$ [deg]	32.3	2.08	53.5	1.93
σ_θ [deg]	31.6	3.25	30.0	1.90

3. Check factors derived from linear wave theory

To compare buoy motions in moored and drifting modes, we analyse two 10-h records taken during stable wave conditions. The first record begins at 00:00 h on 1 November 2019, while the second starts at 18:30 h on 27 April 2020. Stability for these conditions is primarily defined by almost constant H_s and T_z values. Secondary stability factors include the mean wave direction $\overline{\theta}$ and directional spreading σ_θ. The 30-min bulk parameters, along with hourly and total average PSDs, $S_{\eta\eta}(f)$, are illustrated in Fig. 13. (Another superposed comparison of the two heave PSDs averaged from 15-min blocks (40 PSDs) is shown in Fig. 14b.) The mean values and corresponding standard deviations of these bulk parameters are summarised in Table 1. This comparison reveals a slight difference, which may be attributed to either genuine variations as the sea states are from different months or a Doppler shift experienced by the moored buoy.

The first 'check factor' is the depth attenuation factor. According to linear wave theory, the relationship between the depth attenuation factor, $\tanh(kd)$, and the ratio of the signals' PSDs is estimated by

$$\tanh^2(kd) \approx \frac{S_{\eta\eta}(f)}{S_{XX}(f) + S_{YY}(f)}, \tag{3.1}$$

where k is the wavenumber and d is the water depth. Note that S_{XX} and S_{YY} are the PSDs of the easting (X) and northing (Y) signals, respectively. This relation derives from the fact that the PSD, which is a Fourier transform of the autocorrelation function of a signal, is proportional to the square of the amplitude of a wave, and depends on the water depth for horizontal linear signals. For further details on the transformation of time-series signals to PSDs, refer to Ochi (1990, §10). The $\tanh(kd)$ arises as the ratio of vertical to horizontal wave displacements at the still water level in linear wave theory. In deep water, as for this buoy deployment, this check factor should be unity indicating circular linear orbital motions.

The second 'check factor' is the coherence function between the vertical displacement and the horizontal displacement along the mean wave direction, effectively representing surge motions. This signal is obtained from a rotation of the horizontal x–y plane about the mean wave direction $\overline{\theta}$, i.e., $\mathcal{X} = X\cos\overline{\theta} + Y\sin\overline{\theta}$. The coherence function $\gamma^2_{\mathcal{X}\eta}(f)$ measures the degree of linear correlation between two signals at a given frequency, f. It is defined as the squared magnitude of the cross-spectral density normalised by a product of the PSDs of the individual signals:

$$\gamma^2_{\mathcal{X}\eta}(f) = \frac{|S_{\mathcal{X}\eta}(f)|^2}{S_{\mathcal{X}\mathcal{X}}(f)\cdot S_{\eta\eta}(f)}, \tag{3.2}$$

where $S_{\mathcal{X}\eta}$ represents the cross-spectral density between the surge $\mathcal{X}$ and heave η signals. High coherence values approaching unity indicate a strong correlation between the vertical and horizontal displacements at that frequency, suggesting that the wave motion adheres to linear wave theory. Conversely, low coherence values might indicate noise, the presence of multiple wave systems, or other complexities such as

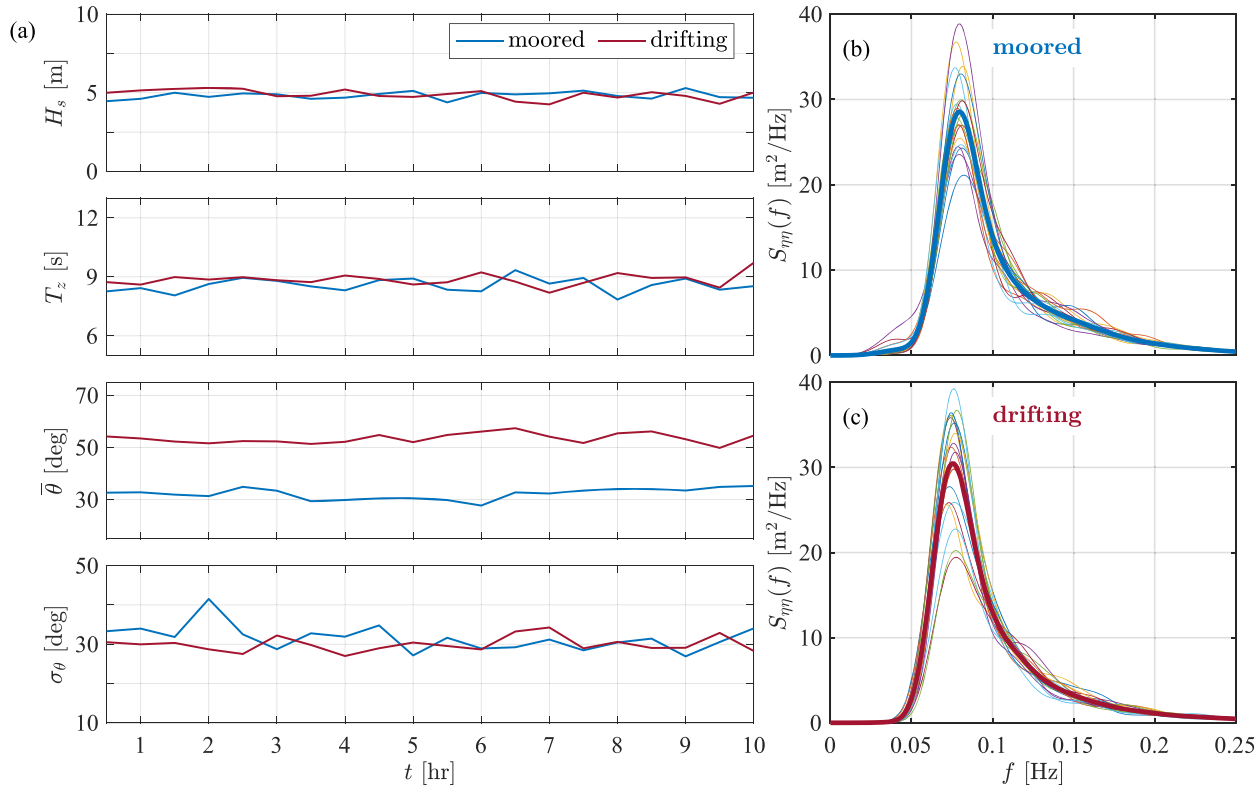

Fig. 13. (a) Bulk wave parameters (H_s, T_z, mean wave direction $\overline{\theta}$, and directional spreading angle σ_θ) for each 30-min sea state from 10-h stable and energetically matched wave conditions during moored and drifting modes. Sea-state PSDs overlaid with their average, plotted in thick lines, for (b) moored and (c) drifting buoy modes.

nonlinear effects. The coherence function is analogous to the correlation coefficient but is frequency-dependent (see Ochi, 1990, §14).

This study uses the coherence function as a diagnostic tool to evaluate the reliability of the directional spreading calculations. High coherence between vertical and horizontal displacements ensures that the derived directional Fourier coefficients (see e.g., Borgman, 1969; Mitsuyasu et al., 1980; Long, 1980) accurately represent the wave field, leading to more accurate estimates of the mean wave direction and directional spreading width. The mean wave direction is mathematically expressed as

$$\overline{\theta} = \tanh^{-1}\left(\frac{Q_{\eta Y}}{Q_{\eta X}}\right), \tag{3.3}$$

where $Q_{\eta\zeta}$ represents the quadrature spectrum of the η and $\zeta \in \{X, Y\}$ time-series signals. The coherence function (3.2) involves both the co-spectrum and quadrature spectrum. According to Tucker and Pitt (2001, §4), the mean wave direction $\overline{\theta}$ corresponds to zero coherence between the heave displacement and the horizontal displacement perpendicular to $\overline{\theta}$, a relationship applied in this analysis.

The 10-h sea states are divided into 40 blocks of 15 min each to estimate the check factors described above, with the final value obtained by averaging over all 40 blocks. The 15-min records, rather than the 30-min records used elsewhere, are chosen to increase the number of samples and improve the accuracy of the averaging process. Fig. 14 demonstrates that the wave buoy performs similarly when both moored and drifting. Panel (a) shows that the drifting buoy closely follows the water particle motion, even at frequencies exceeding $2f_p$, the spectral peak frequency, demonstrating strong agreement with the $\tanh(kd)$ factor. Panel (b) highlights similar levels of coherence between the moored and drifting modes, suggesting that both configurations effectively capture the wave dynamics across a range of frequencies. The observed linear decay in the coherence curves suggests a strong correlation in long waves. Conversely, low coherence values for short-wave components indicate poor correlation, possibly due to noise, multiple wave systems, or nonlinear effects.

4. NewWave-type analysis

The NewWave represents the average shape of the largest wave events extracted from a Gaussian-distributed sea state. Mathematically, the NewWave has been shown to be a scaled autocorrelation function (Lindgren, 1970), which is the inverse Fourier transform of the PSD. This concept is particularly relevant for predicting (e.g., Tromans et al., 1991) and analysing (Zhao et al., 2018) extreme wave loading on offshore structures. According to Jonathan and Taylor (1997), the simple NewWave result applies to large waves in a time series record with amplitudes exceeding twice the standard deviation of the record. For small waves, the average shape is more complex, though still related to spectral properties.

We investigate the buoy motions induced by large waves, focusing on both linear and nonlinear harmonics, as well as the buoy's trajectory as a particle-following sensor. Large waves carry significant energy, making them critical drivers of offshore dynamics. As such, their impact on offshore operations, including structural loading and buoy motions, is far more pronounced compared to smaller waves. Hence, we investigate buoy responses under large wave conditions. To this end, we use two closely matching sea states, in terms of wave height and period, as discussed in Section 3. These records are 10 h long, covering periods when the buoy was moored and drifting. Fig. 13 displays bulk parameters, including significant wave height H_s, mean period T_z, mean direction $\overline{\theta}$ (measured anticlockwise from the east), and the mean directional spreading parameter σ_θ, which represents the standard deviation of a Gaussian function. The directional parameters are energy-weighted, i.e., the average of a parameter $\alpha(f)$ is given by

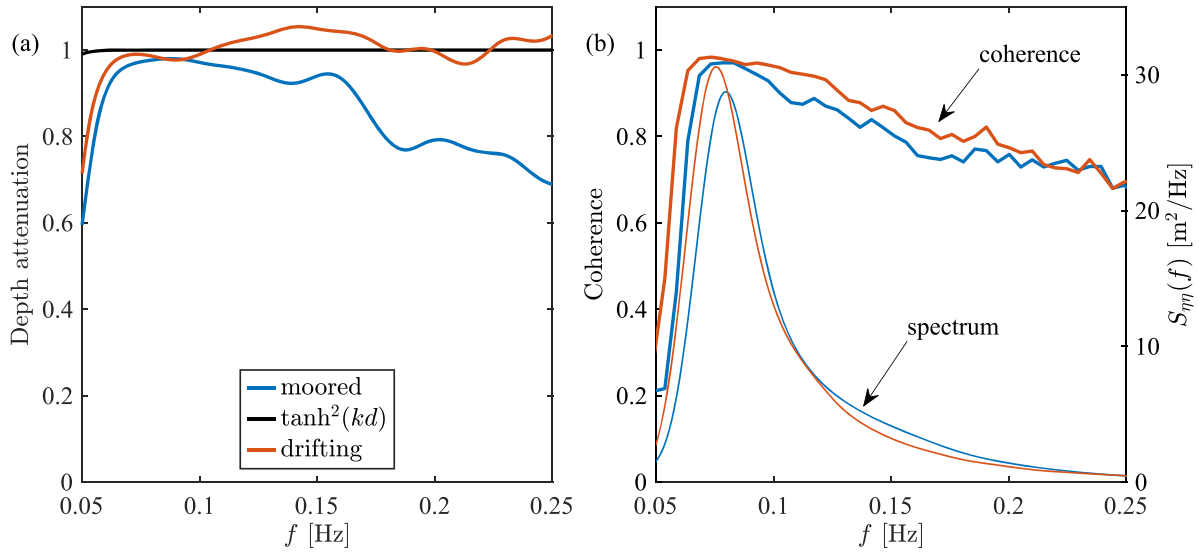

Fig. 14. (a) Depth attenuation function, $\tanh^2(kd)$, approximated by the ratio of the PSDs of heave η and the two horizontal displacements, easting X and northing Y: $\tanh^2(kd) \approx S_{\eta\eta}/(S_{XX}+S_{YY})$. (b) Coherence factor: $\gamma^2_{\mathcal{X}\eta} = |S_{\mathcal{X}\eta}|^2/(S_{\mathcal{X}\mathcal{X}} \cdot S_{\eta\eta})$, where $\mathcal{X}$ is a signal from a rotation of the horizontal x–y plane about the mean wave direction $\overline{\theta}$. The blue lines in both panels represent moored cases and the red lines represent drifting cases. The PSDs from η records overlay in (b), with the y-axis on the right.

$\overline{\alpha} = \int S_{\eta\eta}(f)\alpha(f)\mathrm{d}f / \int S_{\eta\eta}(f)\mathrm{d}f$. Additionally, the PSDs for individual sea states, with their averages overlaid in thick lines within each case, are shown in Fig. 13. A small peak below 0.05 Hz is observed in some PSDs, which can be attributed to the effect of spikes. Only a single spike in the 7th 30-min block is detected by our algorithm in Section 2.2. Therefore, the peaks in the rest of the block PSDs are likely due to long waves that fall just below our threshold. Other than the small long-wave peak, the PSDs during the moored and drifting modes appear similar.

4.1. Harmonic separation

To investigate the presence of nonlinear bound harmonics, we analyse the surge $\mathcal{X}$ (along $\overline{\theta}$), sway $\mathcal{Y}$ (perpendicular to $\overline{\theta}$), and heave η signals separately. This results in a total of six signals: three for the moored mode and three for the drifting mode. Individual waves are identified using a zero up-crossing analysis, resulting in 3,620–5,760 individual zero-crossings. For each signal, the magnitudes of crest and trough displacements are classified, sorted in ascending order, and then compared. Fig. 15 presents parametric plots of sorted crests versus sorted troughs for η, $\mathcal{X}$ and $\mathcal{Y}$, along with their respective Hilbert transforms: η_{H}, $\mathcal{X}_{\mathrm{H}}$ and $\mathcal{Y}_{\mathrm{H}}$, in the lower panels. The Hilbert transform, which applies a 90° phase shift to each signal, is used to reveal the second-order horizontal components—further details are provided below. The colour-coded dashed lines indicate the onset of the 10 % largest waves, where systematic deviations from the $1:1$ line highlight nonlinearity in the wave field.

The η signal is mostly linear, as expected due to the deep water where the buoy was located. In contrast, the $\mathcal{X}$ signal, which is the largest in the horizontal plane, exhibits significant nonlinearity. However, this nonlinearity is evident in the Hilbert transform of the signal, as second-order harmonics—the most prominent nonlinear harmonics—not significantly alter the size of the linear crests and troughs in the horizontal plane. Stokes second-order wave theory provides insight into this behaviour. According to Stokes (1847), the linear vertical component can be written as $\eta^{(1)} \propto \cos\psi$, where $\psi = \psi(x,t)$ is the phase, and the second-order sum term as $\eta^{(2+)} \propto \cos 2\psi$. In the time series $\eta = \eta^{(1)} + \eta^{(2+)}$, the terms on the right-hand side are in phase with each other, with $\eta^{(2+)}$ peaking at both the crests and troughs of $\eta^{(1)}$. The horizontal linear component, $X^{(1)} \propto \sin\psi = \cos(\psi - 90°)$, lags $\eta^{(1)}$ by 90°. The horizontal second-order sum term,

$$X^{(2+)} \propto \sin 2\psi = \cos(2\psi - 90°) = \cos(2[\psi - 90°] + 90°),$$

leads $X^{(1)}$ by 90°. The second-order difference term follows directly from the result of the sum term, lagging $X^{(1)}$ by $\sim 90°$:

$$X^{(2-)} \propto \cos([\psi_1 - \psi_2] - 90°) = \cos([\psi_1 - 90°] - [\psi_2 - 90°] - 90°),$$

for phases $\psi_1 \neq \psi_2$. This explains why the peaks of the second harmonic do not significantly modify the shape of the crests and troughs of the linear $X^{(1)}$.

Applying the Hilbert transform on $X = X^{(1)} + X^{(2)}$ aligns the phases between the linear and second-order terms in the horizontal plane. This alignment is evident in the Hilbert-transformed surge signal, $\mathcal{X}_{\mathrm{H}}$, which displays the expected crest-trough asymmetry (see Fig. 15e). In contrast, the horizontal component perpendicular to the mean wave direction, $\mathcal{Y}$, is weak and prone to noise, making the effect of the Hilbert transform negligible. Therefore, further analysis will focus on the large $\mathcal{X}$ signals.

Employing NewWave analysis, we compare the average sizes of the linear and second-order components in each data stream, analogous to the approach of Ding et al. (2023). Note that the NewWave approximation represents the average shape of the largest wave events contained within a Gaussian sea state. We identify and extract the largest 10 % crests and troughs from the 10-h records to estimate the average shapes of crests and troughs. The extracted segments are 60 s long, with ±30 s away from the highest (deepest) point of a crest (trough). These extreme points are assigned a relative conditioning time $t = 0$.

The separation of harmonics relies on the classical Stokes expansion, in terms of the steepness parameter ka, where k is the wavenumber and a is the linear amplitude. For instance, assuming deep water regular wave conditions, the crest and trough up to the second order can be expressed as

$$\eta_{\mathrm{cr}} = a\cos\psi + \frac{1}{2}ka^2\cos 2\psi + \mathcal{O}\big((ka)^3\big), \tag{4.1}$$

$$\eta_{\mathrm{tr}} = -a\cos\psi + \frac{1}{2}ka^2\cos 2\psi + \mathcal{O}\big((ka)^3\big). \tag{4.2}$$

In tank experiments, the trough signals in (4.2) can be generated by multiplying the paddle signals by −1, resulting in a phase shift

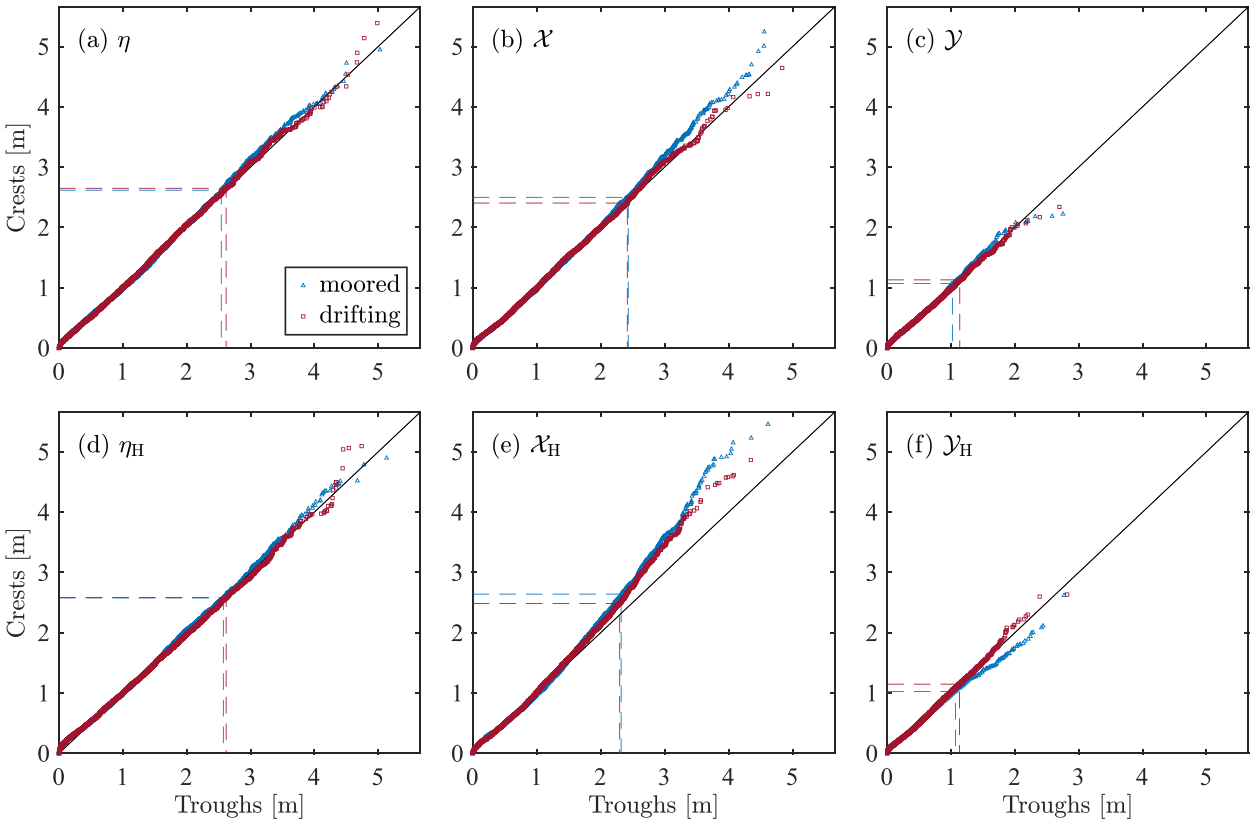

Fig. 15. Ordered crest elevations versus ordered trough depressions for the two 10-h sea states when the buoy was moored (blue triangles) and drifting (red squares). Shown are crests versus troughs for (a) heave η, (b) surge $\mathcal{X}$, along the mean wave direction $\bar{\theta}$, and (c) sway $\mathcal{Y}$, perpendicular to $\bar{\theta}$, as well as (d–f) their respective Hilbert-transformed versions. The vertical and horizontal dashed lines mark the beginning of the largest 10 % troughs and crests.

$\psi \to \psi + \pi$ in (4.1). This inversion alters the signs of all odd harmonics. In random wave data, average crests $\overline{\eta_{\mathrm{cr}}}$ and average troughs $\overline{\eta_{\mathrm{tr}}}$ can be used instead. A subtraction, $(\overline{\eta_{\mathrm{cr}}} - \overline{\eta_{\mathrm{tr}}})/2$, yields the odd harmonics, while an addition, $(\overline{\eta_{\mathrm{cr}}} + \overline{\eta_{\mathrm{tr}}})/2$, yields the even harmonics. These are dominated by first-order and second-order interactions, which are the focus of this work. Given the moderate steepness $k_z H_s \in \{0.265, 0.252\}$ (calculated in the time domain as detailed in Section 2.2) for both moored and drifting buoy cases, the phase manipulation retains predominantly linear $\overline{\eta}^{(1)}$ and second-order $\overline{\eta}^{(2)}$ terms, with low-pass filtering at $3.5 f_p$. This separation applies to all 3-DoF signals. For a detailed discussion on harmonics separation, see Baldock et al. (1996) for the separation of even and odd harmonics or Fitzgerald et al. (2014) for separation up to the fourth-order harmonic using four-phase simulations of the same signal.

Fig. 16 presents the average shapes of the first-order and second-order terms for η and $\mathcal{X}$ for both the moored and drifting modes. Note that two y-axis scales are used: the left scale represents linear terms, while the right scale represents second-order terms. Since the peaks of the (2−) and (2+) components are sufficiently separated in the frequency spectrum, they are isolated using band-pass filtering over $[0, 1.5] f_p$ and $[1.5, 3.5] f_p$, respectively. Panels (a) and (b) of Fig. 16 show that the second-order harmonics in the horizontal $\mathcal{X}$ displacement are larger compared to the vertical η displacement. This observation is consistent with the findings of Ding et al. (2023) for a Datawell buoy moored in intermediate water. Although the second harmonics are significantly smaller vertically due to the deep water, the superharmonics in panel (a) are in phase with the linear component for both drifting and moored conditions, as expected for η. The difference terms $\overline{\eta}^{(2-)}$ are too small and the pattern is not clear, but there is a small set-up (set-down) visible under the linear crest for the moored (drifting) case. The set-up observed in $\overline{\eta}^{(2-)}$, indicative of the buoy's behaviour as a close-to-Lagrangian sensor (see e.g., McAllister and van den Bremer, 2019), was also noted by Ding et al. (2023) for a moored buoy.

Horizontally, there is no significant difference between the moored and drifting Spotter. Panel (b) illustrates the phase misalignment between the second-order $\overline{\mathcal{X}}^{(2\pm)}$ and the linear $\overline{\mathcal{X}}^{(1)}$ average profiles at the conditioning time, $t = 0$. The subharmonics $\overline{\mathcal{X}}^{(2-)}$ lag behind the linear crest by $\sim 90°$, while the superharmonics $\overline{\mathcal{X}}^{(2+)}$ lead it by $\sim 90°$. The shape of the second-order terms, peaking near the zero crossings of the free waves, justifies the absence of modification to the overall horizontal wave peak values presented in Fig. 15b.

4.2. Reciprocity between heave and surge motions

We explore the relationship between the two linear signals: the vertical displacement $\overline{\eta}^{(1)}$ and the horizontal displacement along the mean wave direction $\overline{\mathcal{X}}^{(1)}$. If the coupling between these signals is linear, reciprocity should be observed. In this context, reciprocity refers to whether the characteristics of one displacement can be inferred from the characteristics of the other (see e.g., Zhao et al., 2018; Ding et al., 2023). To this end, we perform a conditioning analysis between two signals, where the largest 10 % of zero-crossing waves in the first signal are identified and extracted. Corresponding portions in time of the second (conditioned) signal are extracted based on the zero crossings from the first (conditioning) signal. The extracted waveforms for each signal are then averaged to analyse the coupling between the two signals. PSDs of the two signals are derived separately from the displacements, and RMS standard deviations are estimated from the zeroth moment m_0 of the spectrum: $\sigma_\eta = \sqrt{m_0(\eta)}$ and $\sigma_{\mathcal{X}} = \sqrt{m_0(\mathcal{X})}$.

The ratio of horizontal to vertical significant wave heights, $\xi_{\mathcal{X}} = \sigma_{\mathcal{X}}/\sigma_\eta$, is used to scale the conditioned $\overline{\eta}^{(1)}$. Reciprocity is then

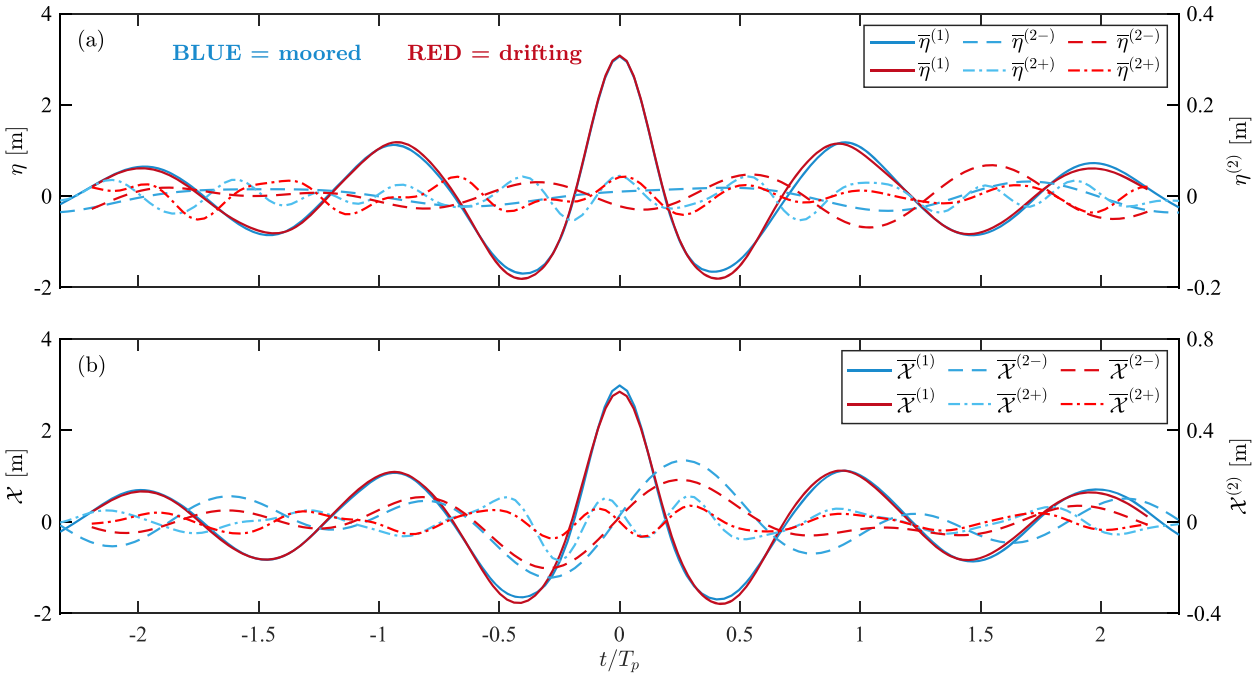

Fig. 16. Decoupled linear (1) and second-order harmonics (2±) for (a) heave η and (b) surge $\mathcal{X}$ displacements (aligned with the mean wave direction). The y-axis for the linear components is on the left, while it is on the right for the second-order harmonics. Note that the t/T_p axes differ; in practice, a 90-degree phase shift exists between the peaks of η and $\mathcal{X}$, as explained in the text.

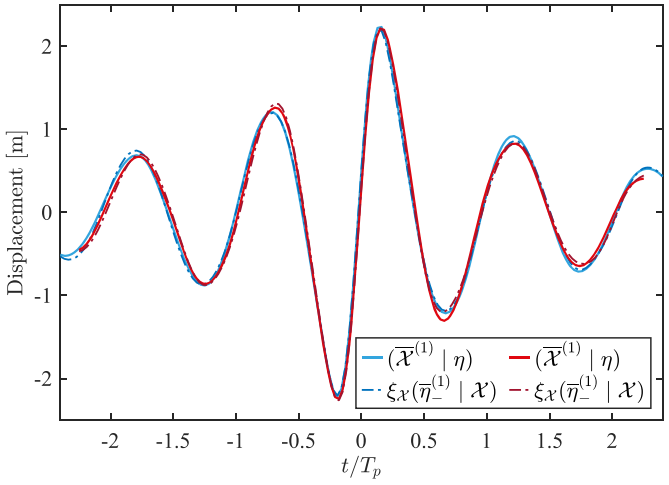

Fig. 17. Reciprocity between the conditioned surge and heave displacements: $(\overline{\mathcal{X}}^{(1)} \mid \eta)$ and $(\overline{\eta}_{-}^{(1)} \mid \mathcal{X})$. Blue lines represent the moored buoy record, and red lines represent the drifting period.

expressed as

$$(\overline{\mathcal{X}}^{(1)} \mid \eta) = \xi_{\mathcal{X}} \times (\overline{\eta}_{-}^{(1)} \mid \mathcal{X}),$$

where subscript (−) indicates reversed time. The vertical line '$(A \mid B)$' reads 'A given B meaning A conditioned on B,' where A and B are dummy variables representing signals.

The analysis reveals an excellent agreement between the conditioned signals, as shown in Fig. 17. This suggests a strong coupling between the linear vertical and linear horizontal displacements, implying that the average horizontal displacement can be inferred from the vertical displacement and vice versa. The near-identical curves for the moored and drifting modes highlight that the two sea states being analysed are almost indistinguishable in an average sense.

4.3. Average buoy trajectories

To assess the similarity in the average buoy trajectories, we explore 10×1-h blocks from each of the 10-h sea states, conditioned on crest elevations denoted by η_{cr}. For each block of the buoy 3D time histories (η, X, Y), the largest 10 % of waves were identified and extracted based on the largest η crests. Fig. 18 shows parametric plots of the hourly average buoy motions for both the moored and drifting modes. Note that no linearisation is applied at this stage. Panels (a) and (d), which show the horizontal x–y plane, illustrate the stability of the sea states relative to wave direction over the 10 h. Additionally, $(\overline{\eta} \mid \eta_{\text{cr}})$ is equivalent to $\overline{\eta}$. The consistent hourly vertical planes shown in panels (b), (c), (e), and (f) result from the stability of both the mean wave direction $\overline{\theta}$ and the directional spreading σ_θ, as indicated in Fig. 13.

Further analysis focuses on the total average buoy trajectory, specifically comparing moored and drifting conditions. These trajectories are inspired by the experimental results of van den Bremer et al. (2019); Calvert et al. (2019), who examined particle trajectories at different depths below a free surface wave group. Their results show a clockwise particle motion with a positive net drift near the surface due to Stokes drift and a negative drift near the bottom due to return flow, for waves travelling from left to right as seen by a stationary observer.

The current analysis treats the data similarly to Section 4.1, but conditioning is based on the heave signal, η, as well as the surge signal, $\mathcal{X}$. Subscripts 'cr' or 'tr' are used where conditioning is based solely on crests or troughs, otherwise, no subscript is used when both crests and troughs are simultaneously considered. The aim is to visualise the path in the vertical plane aligned with $\overline{\theta}$, to mitigate the directionality effects. Fig. 19 shows the complex paths followed by the buoy when measuring large waves. Time is represented by colour for the moored buoy, while thin grey lines are used for the drifting buoy, but follow the same clockwise rotation as the moored buoy. Panels (a) and (b) compare nonlinear surge-heave motions conditioned on η crests and troughs, respectively, with panel (b) having an inverted y-axis. There is a significant lack of symmetry in the shapes, noticeably larger than in the intermediate water results of Ding et al. (2023). There is slightly more asymmetry in the

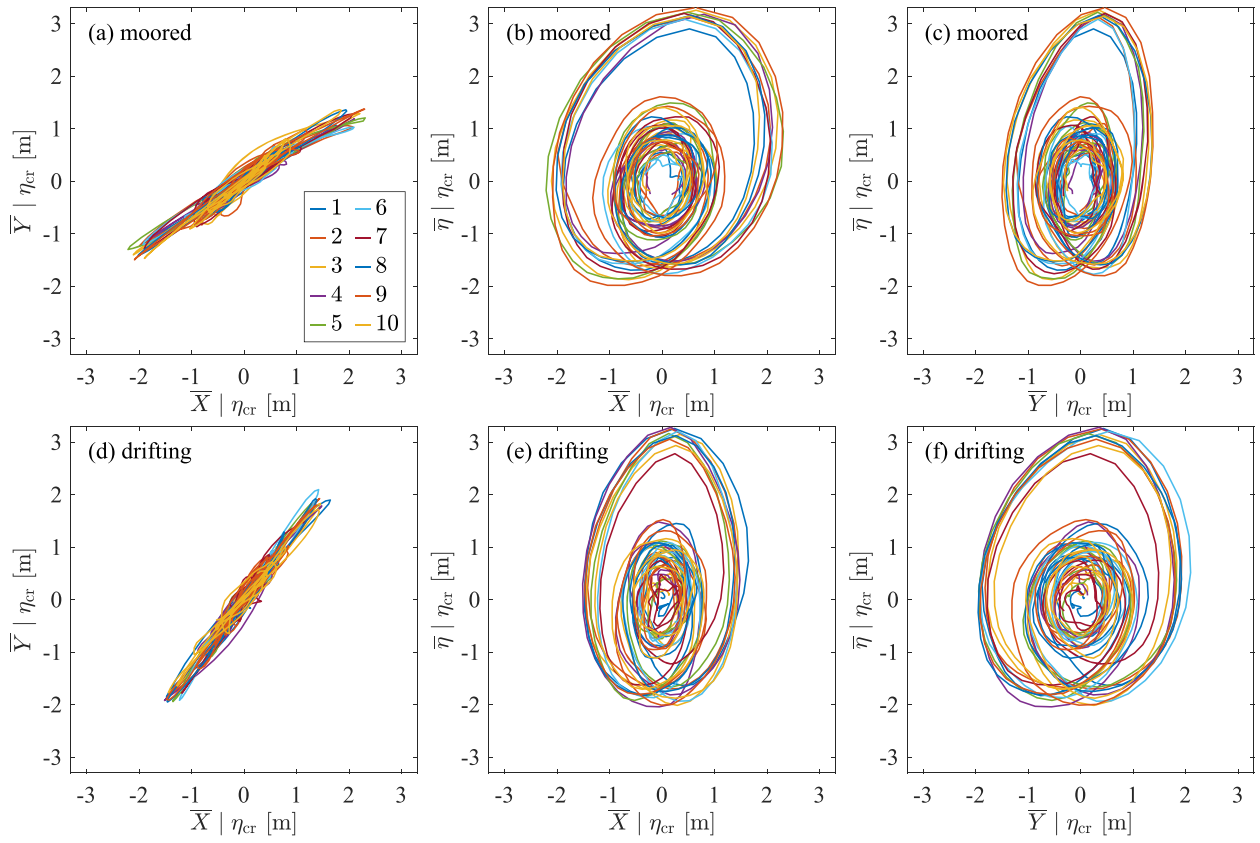

Fig. 18. Parametric plots of the averages of the largest waves in each hourly record for easting $\mathcal{X}$, northing $\mathcal{Y}$, and heave η, all conditioned on the largest η crests. Panels (a–c) show results for the moored buoy, and panels (d–f) for the drifting buoy.

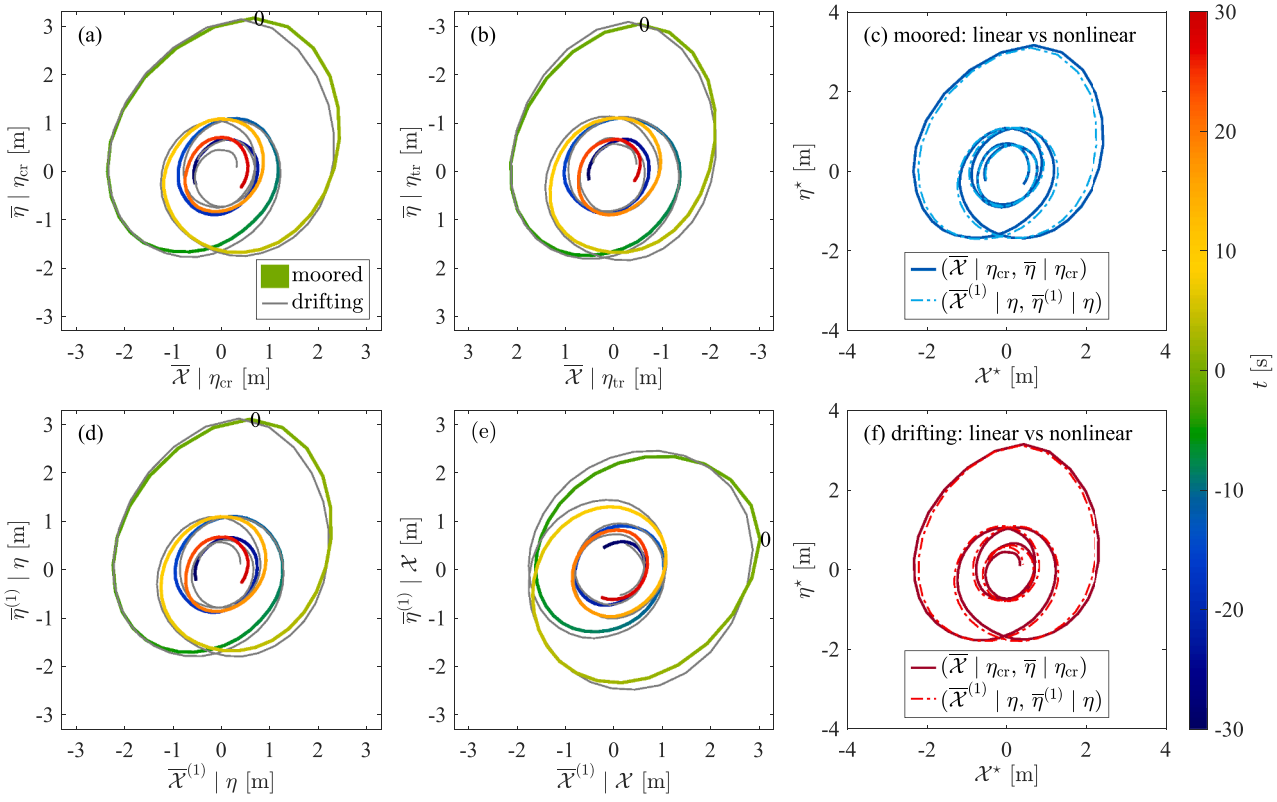

Fig. 19. Average (over 10 h) parametric plots associated with heave η and surge $\mathcal{X}$ displacements. Colour maps in (a,b,d,e) represent the time for the moored records, while the superposed thin grey lines for the drifting buoy follow the same time sequence and exhibit similar clockwise rotation. Panels (c,f) compare buoy paths for linear (1) and nonlinear waves.

moored buoy signals, which may be attributed to the slight differences in the PSDs (see Fig. 13). Panels (d) and (e) show linear surge-heave motions conditioned differently on η and $\mathcal{X}$ signals, respectively. The same level of asymmetry is observed, but the linear case (d) is narrower than its nonlinear counterpart (a), potentially due to the removal of the horizontal nonlinear harmonics, despite their out-of-phase nature relative to the linear displacement. This comparison between linear and nonlinear cases is evident in panels (c) and (f), with no significant vertical difference as the second-order harmonics are very small.

The primary conclusion of this study is that the buoy exhibits similar behaviour when interacting with large waves, whether it is drifting or moored. However, the observed asymmetry in the average wave shapes in the $\mathcal{X}$–η plane remains unresolved and will be the focus of future investigations.

5. Discussion and conclusion

A unique field dataset collected by a Sofar Spotter buoy was used to assess the buoy's performance in both moored and drifting configurations. Besides the significant difference in signal spike counts, the results of the analysis revealed minimal differences between the two configurations. Although these spikes can introduce serious errors in bulk wave parameters, they can be effectively identified and corrected to ensure accurate wave measurement statistics. This provides confidence in the buoy's reliability for both moored and drifting applications when appropriate spike correction protocols are applied. The study focused on two main aspects: detecting and correcting erroneous time-domain signal spikes, and comparing the buoy's motions in both configurations. These findings offer valuable insights into the accuracy and robustness of wave measurements obtained from the Spotter buoy.

Key findings from this study include:

1. Detection and correction of signal spikes: Both moored and drifting configurations of the single buoy exhibited displacement spikes, leading to significant overestimations of the significant wave height (H_s) and spectral peak wave period (T_p), along with slight overestimations of the mean wave period (T_z). We developed a robust method for detecting and correcting these spikes. On average, spikes occurred in 30-min sea states at rates of (0.035, 0.075, 0.035) for east, north and vertical displacements for moored mode, and (0.029, 0.039, 0.019) for drifting mode. During steep wave conditions, $k_z H_s \in [0.3, 0.35)$, the east and north spikes increased to (0.2, 0.6) when moored and (0.08, 0.8) when drifting, while vertical displacements remained largely unaffected. This de-spiking protocol could significantly improve the accuracy of bulk wave parameter estimation and real-time data correction, provided it is integrated into onboard processing and/or real-time displacement data reprocessing.
2. Consistency with linear wave theory: When drifting, the buoy motion and observations were in better agreement with linear wave theory. This included a comparison of $\tanh(kd)$ check, where k is the wavenumber and d is the water depth. This factor is a dimensionless parameter that provides insight into the nature of the waves relative to the water depth. The drifter benefited from the ability to act as a full Lagrangian sensor in the open ocean. In contrast, the moored case, influenced by the tension in their mooring lines, exhibited data that could be slightly biased by these constraints.
3. Average buoy trajectories: The analysis of buoy paths in both moored and drifting states demonstrated a consistent clockwise spiral motion with similar vertically asymmetric trajectories. Subtle differences were observed between the linearised and fully nonlinear trajectories under linear and nonlinear wave conditions.
4. Decoupled wave harmonics: The NewWave-type analysis showed that the buoy had similar capability for measuring large waves in both moored and drifting configurations. The average shape of the first and second harmonics appeared consistent between the two deployment modes, indicating that both configurations can effectively capture key wave characteristics.

Overall, this study emphasises the importance of addressing measurement errors and understanding the operational dynamics of buoys in different configurations. The findings contribute to improving the accuracy of wave data collected by Sofar Spotter buoys and lay a strong foundation for future research in buoy-based wave measurement systems. While our analysis focuses on the Spotter buoy, the findings and de-spiking protocol may have broader implications for other GPS-based wave buoys, potentially enhancing the accuracy of real-time wave data processing and bulk parameter estimation.

While our spike removal approach significantly improves bulk wave statistics, applications requiring complete wave-by-wave information, such as phase-resolved wave prediction (e.g., Chen et al., 2024), may need further refinement. Nonetheless, the consistency in measurement quality between moored and drifting Spotter buoys highlights their reliability across varying deployment scenarios. These results contribute to ongoing advancements in wave measurement technologies and may inform the future design of next-generation microbuoys for oceanographic applications.

Declaration of competing interest

The authors declare that they have no known competing financial interests or personal relationships that could have appeared to influence the work reported in this paper.

CRediT authorship contribution statement

Thobani Hlophe: Writing – review & editing, Writing – original draft, Visualization, Software, Methodology, Formal analysis, Conceptualization; **Paul H. Taylor:** Writing – review & editing, Methodology, Formal analysis, Conceptualization; **Jeff E. Hansen:** Writing – review & editing, Project administration, Methodology, Formal analysis; **Hugh Wolgamot:** Writing – review & editing, Project administration, Funding acquisition; **Michael V.W. Cuttler:** Writing – review & editing, Data curation.

Acknowledgements

Funding for the data collection was provided by Australia's Integrated Marine Observing System (IMOS) New Technology Proving program. The authors acknowledge support from the Shell Chair in Offshore Engineering at The University of Western Australia, which is sponsored by Shell Australia.

Appendix A. Pseudocode for the de-spiking procedure

This appendix presents the pseudocode for the de-spiking algorithm outlined in Section 2.2. The de-spiking procedure is designed to identify and remove anomalous wave displacements, or 'spikes,' from wave displacement records. These spikes can distort the calculation of key wave parameters, including significant wave height (H_s), mean zero-crossing period (T_z), peak period (T_p) and wave direction (θ). The algorithm operates iteratively, using criteria based on the magnitude of displacement and the curvature of the wave to flag outliers for removal.

The full pseudocode implementation for the procedure applied to η is presented below in Algorithm 1. In practice, the algorithm can be adapted for the other signal components, X and Y, where de-spiking is based on T_z values derived from η.

In addition to the primary de-spiking steps, several optional manipulations can be incorporated. For example, the power spectrum can be

computed from the longest continuous record segments that do not contain spikes. This can be useful when deriving spectral quantities like T_p and θ, which can be computed with comparable accuracy to the full-length record (Dhoop et al., 2024).

Algorithm 1 Spike detection and removal in heave, $\eta(t)$.

Input:
  $\eta(t) = [\eta_1, \eta_2, \dots, \eta_N]$: wave elevation time series
  $t = [t_1, t_2, \dots, t_N]$: sampling time
  $T_{\text{spike}} = 30$ s: time window for spike removal
Output: Processed bulk wave statistics: H_s, T_z, $T_{\max}$, etc.
Define parameters:
  $\mathcal{K}$: curvature
  H, H_s: wave height, significant wave height
  T, T_z: wave period, mean period
  $\eta_{\text{cr}}, \eta_{\text{tr}}$: crest height, trough depth
  σ_ζ: RMS standard deviation for a signal ζ
Define detection thresholds:
(1) A wave is a spike if $H > 2.20H_s$ **AND** $\mathcal{K} > 5\sigma_{\mathcal{K}}$, **OR** $H > 3H_s$
(2) A crest/trough is a spike if $|\eta| > 1.25H_s$ **AND** $\mathcal{K} > 5\sigma_{\mathcal{K}}$, **OR** $|\eta| > 1.7H_s$
(3) A wave period is anomalous if $T > \min(3.5T_z, 30)$
Preprocess signal:
Compute curvature numerically: $\mathcal{K}_i \approx \left(\eta_{i+1} - 2\eta_i + \eta_{i-1}\right)/\Delta t^2,\ \forall\ 1 \leq i \leq N$
Identify zero-crossing points (both *up* and *down*): $t_0, t_1, \dots, t_M, t_{M+1}$
Compute initial wave parameters:
Initialise vectors of length M: $\boldsymbol{\eta}_{\text{cr}}, \boldsymbol{\eta}_{\text{tr}}, \mathbf{H}, \mathbf{T}, \mathbf{K}$
for each wave segment i between up or down zero-crossings **do**
    Identify crest $\eta_{\text{cr},i}$ as the global maximum of the wave segment
    Identify trough $\eta_{\text{tr},i}$ as the global minimum of the wave segment
    Compute wave height: $H_i = \eta_{\text{cr},i} - \eta_{\text{tr},i}$
    Compute wave period: $T_i = t_i - t_{i-2}$
    Compute curvature: $\mathcal{K}_i = \max(|\mathcal{K}(t)|),\ \forall\ t_{i-2} \leq t < t_i$
end for
Compute significant wave height: $H_s = 4\sigma_\eta$
Compute zero-crossing period: $T_z = \text{mean}(\mathbf{T})$
Iterate to detect and remove spikes:
repeat
    Initialise spike location vector $\mathbf{t}_{\text{spike}}$
    for each wave segment i between zero-crossings **do**
        Identify spikes based on threshold conditions: $\{H_i, T_i, \eta_{\text{cr},i}, \eta_{\text{tr},i}, \mathcal{K}_i\}$
        if spike detected **then**
            Append $t_{\text{spike},i}$ (location of min/max η) to $\mathbf{t}_{\text{spike}}$
        end if
    end for
    Remove η values in range: $-T_{\text{spike}} \leq t - t_{\text{spike},i} \leq T_{\text{spike}}$
    Update $\mathbf{T}, \mathbf{H}$, etc. after de-spiking
    Recalculate H_s and T_z after de-spiking
until no new spikes detected for two consecutive iterations
Return: Processed wave statistics: H_s, T_z, $T_{\max}$, etc.

References

Baldock, T.E., Swan, C., Taylor, P.H., 1996. A laboratory study of nonlinear surface waves on water. Philos. Trans. R. Soc. Lond. Ser. A 354 (1707), 649–676.
Baschek, B., Imai, J., 2011. Rogue wave observations off the US West Coast. Oceanography 24 (2), 158–165.
Björkqvist, J.-V., Pettersson, H., Laakso, L., Kahma, K.K., Jokinen, H., Kosloff, P., 2016. Removing low-frequency artefacts from Datawell DWR-G4 wave buoy measurements. Geosci. Instrum., Methods Data Syst. 5 (1), 17–25.
Borgman, L.E., 1969. Directional spectra models for design use. In: Offshore Technology Conference. OTC, pp. OTC–1069.
van den Bremer, T.S., Whittaker, C., Calvert, R., Raby, A., Taylor, P.H., 2019. Experimental study of particle trajectories below deep-water surface gravity wave groups. J. Fluid Mech. 879, 168–186.
Calvert, R., Whittaker, C., Raby, A., Taylor, P.H., Borthwick, A.G.L., van den Bremer, T.S., 2019. Laboratory study of the wave-induced mean flow and set-down in unidirectional surface gravity wave packets on finite water depth. Phys. Rev. Fluids 4 (11), 114801.
Chen, J., Hlophe, T., Gunawan, D., Taylor, P.H., Milne, I.A., Zhao, W., 2024. Phase-resolved wave prediction with varying buoy positions in the field using machine learning-based methods. Ocean Eng. 307, 118107.
Cresswell, G.R., Golding, T.J., 1980. Observations of a south-flowing current in the south-eastern Indian Ocean. Deep Sea Res. Part A 27 (6), 449–466.
Cuttler, M. V.W., Hansen, J.E., Lowe, R.J., 2020. Seasonal and interannual variability of the wave climate at a wave energy hotspot off the southwestern coast of Australia. Renew. Energy 146, 2337–2350.
Dhoop, T., Newman, R., Warwick-Champion, E., Thompson, C., 2024. Re-processing Datawell Directional Waverider MkIII heave data affected by breaking waves. In: Proceedings of the Institution of Civil Engineers-Maritime Engineering. Emerald Publishing Limited, pp. 1–7.
Ding, Y., Taylor, P.H., Hlophe, T., Zhao, W., 2024. Comparison of two types of wave buoys: linear and second-order motion. In: International Conference on Offshore Mechanics and Arctic Engineering. Vol. 87820. American Society of Mechanical Engineers.
Ding, Y., Taylor, P.H., Hlophe, T., Zhao, W., 2025. A comparison of linear and nonlinear 3D semi-Lagrangian motion of moored Waverider and Spotter wave buoys. Coastal Eng. 196, 104661.
Ding, Y., Taylor, P.H., Zhao, W., Dory, J.-N., Hlophe, T., Draper, S., 2023. Oceanographic wave buoy motion as a 3D-vector field: Spectra, linear components and bound harmonics. Appl. Ocean Res. 141, 103777.
Dysthe, K., Krogstad, H.E., Müller, P., 2008. Oceanic rogue waves. Annu. Rev. Fluid Mech. 40 (1), 287–310.
Fitzgerald, C.J., Taylor, P.H., Eatock Taylor, R., Grice, J., Zang, J., 2014. Phase manipulation and the harmonic components of ringing forces on a surface-piercing column. Proc. R. Soc. A 470 (2168), 20130847.
Heller, E.J., 2006. Freak ocean waves and refraction of Gaussian seas. In: Extreme Events in Nature and Society. Springer, pp. 189–210.
Hemer, M.A., Zieger, S., Durrant, T., O'Grady, J., Hoeke, R.K., McInnes, K.L., Rosebrock, U., 2017. A revised assessment of Australia's national wave energy resource. Renew. Energy 114, 85–107.
Hisaki, Y., 2021. Validation of drifting buoy data for ocean wave observation. J. Mar. Sci. Eng. https://api.semanticscholar.org/CorpusID:237851279.
Hlophe, T., Taylor, P.H., Kurniawan, A., Orszaghova, J., Wolgamot, H., 2023. Phase-resolved wave prediction in highly spread seas using optimised arrays of buoys. Appl. Ocean Res. 130, 103435.
Holthuijsen, L.H., 2010. Waves in Oceanic and Coastal Waters. Cambridge University Press.
Jonathan, P., Taylor, P.H., 1997. On irregular, nonlinear waves in a spread sea. J. Offshore Mech. Arct. Eng. 119 (1), 37–41. https://doi.org/10.1115/1.2829043
Kurniawan, A., Taylor, P.H., Orszaghova, J., Wolgamot, H., Hansen, J., 2022. Measuring a rogue? An investigation into an apparent giant wave. J. Atmos. Ocean. Technol. 39 (8), 1129–1147.
Lindgren, G., 1970. Some properties of a normal process near a local maximum. Ann. Math. Stat. 41 (6), 1870–1883.
Long, R.B., 1980. The statistical evaluation of directional spectrum estimates derived from pitch/roll buoy data. J. Phys. Oceanogr. 10 (6), 944–952.
McAllister, M.L., van den Bremer, T.S., 2019. Lagrangian measurement of steep directionally spread ocean waves: second-order motion of a wave-following measurement buoy. J. Phys. Oceanogr. 49 (12), 3087–3108.
Mitsuyasu, H., Tasai, F., Suhara, T., Mizuno, S., Ohkusu, M., Honda, T., Rikiishi, K., 1980. Observation of the power spectrum of ocean waves using a cloverleaf buoy. J. Phys. Oceanogr. 10 (2), 286–296.
Sofar Ocean, 2024. Sofar Spotter. https://www.sofarocean.com/products/spotter.
Ochi, M.K., 1990. Applied Probability and Stochastic Processes. Wiley New York.
Stokes, G.G., 1847. On the theory of oscillatory waves. Trans. Camb. Philos. Soc. 8, 411–455.
Tromans, P.S., Anaturk, A.R., Hagemeijer, P., 1991. A new model for the kinematics of large ocean waves-application as a design wave. In: ISOPE International Ocean and Polar Engineering Conference. ISOPE, pp. ISOPE–I.
Tucker, M.J., Pitt, E.G., 2001. Waves in Ocean Engineering. 5. Elsevier.
Veras Guimarães, P., Ardhuin, F., Sutherland, P., Accensi, M., Hamon, M., Pérignon, Y., Thomson, J., Benetazzo, A., Ferrant, P., 2018. A surface kinematics buoy (SKIB) for wave–current interaction studies. Ocean Sci. 14 (6), 1449–1460.
Zhao, W., Taylor, P.H., Wolgamot, H.A., Eatock Taylor, R., 2018. Identifying linear and nonlinear coupling between fluid sloshing in tanks, roll of a barge and external free-surface waves. J. Fluid Mech. 844, 403–434.